RSC Advances

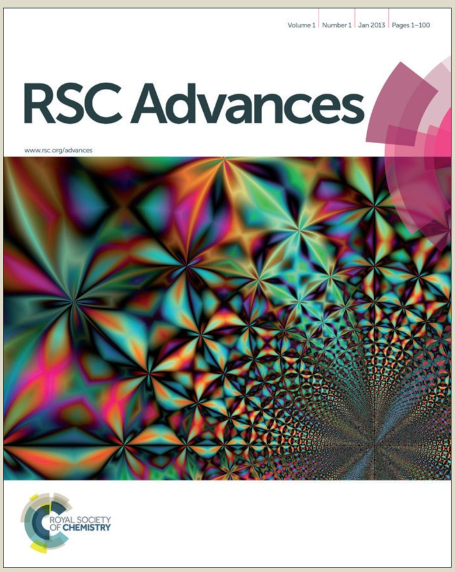

Prediction of Multiphase Flow Pattern inside a 3D Bubble Column Reactor Using a Combination of CFD and ANFIS

M. Pourtousi[a], Mohammadjavad Zeinali[b], P. Ganesan [a] and J. N. Sahu[c]*

[a]Department of Mechanical Engineering, University of Malaya, 50603 Kuala Lumpur, Malaysia
[b]Vehicle System Engineering Laboratory, Malaysia-Japan International Institute of Technology, Universiti Teknologi Malaysia, Jalan Semarak, 54100 Kuala Lumpur, Malaysia
[c]Petroleum and Chemical Engineering Programme Area, Faculty of Engineering, Institut Teknologi Brunei, Tungku Gadong, P.O. Box 2909, Brunei Darussalam

Abstract

This work presents a combination of Computational Fluid Dynamics (CFD) and Adaptive Network-based Fuzzy Inference System (ANFIS) developed for flow characterization inside a cylindrical bubble column reactor. An attempt has been made to predict the liquid flow pattern and gas dynamics for various ring sparger diameters (i.e., 0.07-0.16m) and bubble column heights. Gas hold-up, Turbulent Kinetic Energy (TKE) and axial liquid velocity are the output parameters predicted by using ANFIS method with respect to sparger diameter, axial coordination and radial coordination. Various architectures of the ANFIS method were constructed in order to achieve an accurate prediction model of the liquid flow behavior and gas dynamics inside the bubble column. ANFIS approaches were trained and tested by using CFD simulation results. The performance of the ANFIS approaches was examined by comparing the root mean square error and correlation coefficient values of the prediction models. The CFD simulation results are validated with existing experimental and numerical data and mathematical correlations. Both CFD simulation and ANFIS prediction results show that ring sparger diameter significantly changes the liquid flow pattern and gas dynamics, resulting different amount of the gas inside the column. Different ANFIS structures were selected for precisely estimation of gas hold-up, TKE and axial liquid velocity. Eventually, the mathematical correlations of the proposed ANFIS approaches are presented with correlation coefficients of 0.9717, 0.9917 and 0.9877 for gas hold-up, turbulent kinetic energy and axial liquid velocity prediction models. Hence, ANFIS approach is able to provide a prediction of the 3D bubble column hydrodynamics in a continuous domain.

Keywords: Bubble column reactor; Numerical method; Soft computing; CFD; ANFIS; Multiphase flow

Nomenclature

C_D	Drag force coefficient (-)
C_{TD}	Turbulent dispersion coefficient (-)
$C_{\varepsilon 1}$	Model parameter in turbulent dissipation energy equation (-)
$C_{\varepsilon 2}$	Model parameter in turbulent dissipation energy equation (-)
C_μ	Constant in k-ε model (-)
$C_{\mu,BI}$	Constant in bubble induced turbulence model (-)
d_B	Bubble diameter (m)
d_0	Sparger hole diameter (m)
D	Diameter of the column (m)
D_S	Sparger diameter (m)
g	Gravitational constant (m/s^2)
G	Generation term ($kg/m\ s^2$)
H	Height (m)
k	Turbulent kinetic energy per unit mass (m^2/s^2)
M_I	Total interfacial force acting between two phases (N/m^3)
M_D	Drag force (N/m^3)
P	Pressure (N/m^2)
r	Radial distance (m)
R	Column radius (m)
Re_B	Reynolds number ($= d_B V_S / v$) (-)
V_G	Superficial gas velocity (m/s)
V_y	Axial liquid velocity (m/s)
TKE	Turbulent kinetic energy
MF	Membership function
RMSE	Root mean square error
Greek Symbols	
ε	Turbulent energy dissipation rate per unit mass (m^2/s^3)
$\in$	Fractional phase hold-up (-)
$\overline{\in}$	Average fractional phase hold-up (-)
μ	Molecular viscosity (Pa s)
μ_{BI}	Bubble induced viscosity (Pa s)
μ_{eff}	Effective viscosity (Pa s)
ρ	Density (kg/m^3)
μ_T	Turbulent viscosity (Pa s)
σ	Surface tension (N/m)
σ_ε	Prandtl number for turbulent energy dissipation rate (-)
σ_k	Prandtl number for turbulent kinetic energy (-)
τ_k	Shear stress of phase k (Pa)
ϵ_g	Air fraction / Gas hold-up
Subscripts	
G	Gas phase
L	Liquid phase

1 Introduction

Bubble column reactors are extensively used in several multiphase reaction processes within industrial applications such as chemical, biochemical and wastewater treatment [1-7]. They are preferred over other reactors due to high energy efficiency, low design costs, simple structure and operation [1, 3]. Furthermore, they have a good performance in phase mixing characteristics and heat and mass transfer (large interfacial areas) [1, 3, 8, 9]. They are often cylindrical or rectangular, including gas sparger (gas distributor) at the bottom. The sparger produces bubbles in a continuous liquid phase (stationary or flowing) or a liquid–solid suspension [1, 3, 10-15].

Design, optimization and manufacturing of these reactors highly depend on the complex dynamics of gas bubble interaction, liquid flow pattern and prevailing gas and liquid regime (i.e., homogeneous or heterogeneous) [3, 11-13, 16-20]. One of the main challenges in enhancing the design and manufacturing of the bubble column is to properly predict and measure the hydrodynamics properties, while the complex behavior of the gas and liquid movement, including the interaction between bubbles are unavoidable [1, 3, 11, 12, 15, 21, 22]. Several experimental methods such as Particle Image Velocimetry (PIV), Laser Doppler Anemometry (LDA) and Radioactive Particle Tracking have been developed in recent years to develop an insight into this arguably complex and nonlinear behavior of gas and liquid dynamics, particularly liquid flow pattern and amount of gas inside bubble column reactors [23-26].

Apart from experimental techniques, many CFD approaches and mathematical calculations are available to predict bubble column hydrodynamics [3, 7, 13-15, 27-29]. Nowadays, high performance computers have enabled the use of detailed mathematical and computational approaches to study the liquid flow pattern and gas dynamics on a feasible time span and space. There are two main CFD approaches i.e., the Eulerian–Eulerian and Eulerian–Lagrangian to model multiphase fluid flow [3, 6, 10, 13-15, 19, 27-30]. In the Eulerian–Lagrangian approach (Discrete particle model), each bubble is separately tracked inside the bubble column by solving forces acting on the bubbles, while continuum description is considered for the liquid phase [6]. In this approach, the interaction between bubbles i.e., coalescence, break-up and collisions can be observed. However, this framework is limited for large bubble columns with high number of bubbles due to solving more equations in large domains. On the other hand, Eulerian–Eulerian approach (the two fluid model), considers gas bubbles and liquid in the Eulerian framework as two interpenetrating fluids. Unlike the discrete particle model, the Eulerian framework is an appropriate method to solve the large bubble column with high superficial gas velocity, particularly in industrial bubble column reactors [13-15, 22, 29].

Although several experimental, numerical and mathematical methods have been used to measure and estimate the flow pattern and bubbles dynamics [3, 5-7, 9, 31-39], there are some difficulties to completely predict the liquid flow pattern and gas dynamics (bubble coalescence, break-up, velocity, shape, size and gas hold-up) at each point of 3D bubble column reactors when the operation conditions (i.e., superficial gas velocity, column dimensions, gas and liquid properties and sparger parameters), flow regime and operation time change. For instance, measuring the fluid flow parameters inside the 3D bubble column reactor during experiment is extremely expensive and required much measurement equipment. Computation time and computer capability are the major limitations of the computational approaches in numerically simulation of the large bubble column and various operation conditions. Because of these limitations, soft computing methods have been developed to estimate the bubble column hydrodynamics in various conditions that have not been simulated or experimented at every point of the bubble column [37].

There are several soft computing techniques (e.g., neural networks, Support vector machines, evolutionary algorithms, and adaptive neuro fuzzy inference system) proposed in many studies to estimate phenomena behaviour in the real life applications [37, 40-47]. Among these techniques, Adaptive Network-based Fuzzy Inference System (ANFIS) has attracted researchers because of its ability to learn complex relationships and its vast application has been illustrated in numerous studies [41, 48-50]. The accuracy of the ANFIS approach can be altered by changing prediction model structure and adapted on the basis of the relationship complexity [40, 41, 51-58]. ANFIS method can use either simulation or experimental results as training data to learn the phenomena behavior. An appropriate set of training data is required to successfully train ANFIS model.

Azwadi et al.[41] used CFD results for training ANFIS method to estimate the temperature and flow fields in a 2D lid-driven cavity. They found that the result of ANFIS method is in good agreement with temperature and flow field obtained by CFD simulation. Recently, Pourtousi et al. [37] employed this methodology to predict multiphase flow inside a bubble column reactor. They utilized bubble column hydrodynamics data (i.e., liquid velocity components, turbulent kinetic energy and gas hold-up), obtained by CFD (Eulerian method) simulation, at the bubble column bulk region for ANFIS learning process. It was found that the combination of CFD and

ANFIS is a robust methodology to predict the bubble column hydrodynamics properties in a continuous domain. They showed that ANFIS method can be a favourable replacement with CFD simulation to predict the complex behaviour of multiphase flow inside the bubble column reactor when the flow regime is homogeneous.

In this study we develop the recent methodology (Pourtousi et al.'s research [37]) to propose an intelligent approach which is able to model multiphase flow inside the bubble column reactor for various sparger diameters. In addition, an attempt has also been made to improve the overall predictive capabilities of liquid flow pattern and gas hold-up using the combination of CFD and ANFIS methods. A new mathematical correlation is proposed to predict the bubble column hydrodynamics as the ring sparger diameters varied from 0.07 to 0.16m. The effect of ring sparger diameter on liquid flow velocity, turbulent kinetic energy and gas hold-up is investigated using ANFIS and CFD results. Various ANFIS structures were constructed to realize the most accurate structure for each output. The accuracy of all prediction models was compared by two common error evaluation formulas; root means square error and correlation coefficient. The results of selected ANFIS models were compared to the CFD simulation results to illustrate the capability of the ANFIS approach.

2 Methodologies

2.1 Geometrical structure

In this CFD simulation study, a 3D cylindrical bubble column reactor with 2.6m height and 0.288m diameter is used to produce the multiphase flow (bubbling process). The bubble column is filled with stationary water at ambient condition. At the bottom of the column, 20 similar holes (sparger) whose diameter varied from 0.07 to 0.16 m are symmetrically defined a circle with diameter of 0.7m. The superficial gas velocity for all simulation cases are 0.005m/s, resulting in homogeneous flow regime with almost uniform bubble sizes, shapes and velocities.

2.2 Combination of CFD and ANFIS methods

The prediction of the 3D bubble column hydrodynamics is started by CFD simulation of 10 case studies with different sparger diameters. The CFD simulation results are employed to train the ANFIS approaches. Fig. 1 portrays the schematic of prediction procedure of bubble column using the combination of CFD and ANFIS.

2.3 CFD modeling

In the current CFD simulation study, the Euler–Euler approach as incorporated in the commercial ANSYS CFX-13 software is employed to model the multiphase flow inside the bubble column. The Eulerian framework of the gas and liquid flow represents a point volume fraction for the gas and liquid individually. This method is based on the notion of pseudo-continuum. Both the liquid and gas phases (multi-bubbles) are formulated in the Eulerian framework as interpenetrating continua. The formulations of the Eulerian model, selected in the present CFD study, are based on ensemble-averaged mass and momentum transport equations for the gas and liquid separately. The continuity and momentum transfer equations for the Euler–Euler multi-phase framework are represented respectively (solved for the gas and liquid phases individually) as follows:

The mass conservation equation for both liquid and gas is shown as follows:

$$\frac{\partial}{\partial t}(\rho_k \in_k) + \nabla(\rho_k \in_k u_k) = 0 \quad (1)$$

where $\in_k$ and u_k indicate the volume fraction and average velocity of phase k respectively.

In the present numerical investigation, the control volume method is used to discretize the conservation equations. There are several solution methods (such as finite difference [59], Lattice Boltzmann [60-63], finite volume method [13-15, 27, 28], etc.) in the CFD to solve the fluid flow problems. The most robust, reliable and the one, on which CFX is based, is called finite volume discretization method. Based on the finite volume discretization method, the momentum transfer formulation for multi-bubbles and liquid phases can be described as:

$$\frac{\partial}{\partial t}(\rho_k \in_k u_k) + \nabla(\rho_k \in_k u_k u_k) = -\nabla(\in_k \tau_k) - \in_k \nabla p + \in_k \rho_k g + M_{I,K} \quad (2)$$

The right side of the momentum transfer formulation consists of the stress, pressure gradient, gravity and the momentum interfacial exchange between gas bubbles and liquid. In this equation, the stress term of phase k is represented as follows:

$$\tau_K = -\mu_{eff,k}(\nabla u_k + (\nabla u_k)^T - \frac{2}{3} I(\nabla u_k)) \quad (3)$$

where μ indicates the liquid phase effective viscosity, comprising of three terms: molecular viscosity, turbulence viscosity and viscosity based on bubble induced turbulence.

$$\mu_{eff,l} = \mu_L + \mu_{T,L} + \mu_{\mathrm{BI},L} \quad (4)$$

The effective gas viscosity is formulated based on the effective viscosity of liquid and it can be described as follows:

$$\mu_{eff,G} = \frac{\rho_G}{\rho_L}\mu_{eff,\mathrm{L}} \quad (5)$$

In the current CFD simulation study, the model of Sato and Sekoguchi is employed for the extra term due to bubble induced turbulence, containing a constant value of $C_{\mu,BI} = 0.6$. The viscosity due to the turbulence induced by the gas bubble flow has been described by [64, 65]. They demonstrated a model taking account the turbulence induced by bubble agitation inside the liquid phase. In general, to predict momentum of bubble flow it is crucial to describe the turbulent structure of the continuous liquid phase, which may result in how to describe the contribution of bubble existence to the flow characteristics. Sato and Sekoguchi [64], reported that the turbulent shear stress in bubble flow is affected by two terms. Firstly, the inherent liquid turbulence which is independent of relative motion of bubbles in the liquid phase. Secondly, The additional liquid turbulence term, producing by bubble agitation (bubble motion).

$$\mu_{BI,L} = \rho_L C_{\mu,\mathrm{BI}} \in_G d_B \left|u_G - u_L\right| \quad (6)$$

The last term in the momentum transfer equation is the total interfacial force. This term can be described as follows:

$$M_{I,L} = -M_{I,\mathrm{G}} = M_{\mathrm{D},L} + M_{\mathrm{TD},L} \quad (7)$$

The total interfacial forces, illustrated above, indicate the drag and turbulent dispersion force when the lift and virtual mass are neglected. The interphase momentum transfer between gas bubble and liquid phase due to drag force is shown as follows:

$$M_{D,L} = -\frac{3}{4} \in_G \rho_L \frac{C_D}{d_B}\left|u_G - u_L\right|(u_G - u_L) \quad (8)$$

where the C_D and d_B are the drag coefficient and bubble diameter respectively. In general, the drag coefficient and bubble diameter can be assumed as a constant value due to uniform behaviour of bubble size and shape in homogeneous regime. The drag coefficient and bubble diameter are selected as 0.44 and 4mm diameter, respectively, based on the literature suggestions [3, 13, 14, 37], experimental observation and numerical setting of Pfleger and becker's study [13].

Turbulent dispersion force model is used for current CFD investigations based on literature studies [3, 15, 22, 37, 66] to improve the flow field prediction towards the walls. This model, formulated by Lopez de Bertodano [67], is on the basis of the analogy with molecular movement and interaction. It approximates a turbulent diffusion of the bubbles by the liquid eddies and can be described as:

$$M_{TD,L} = -M_{TD,G} = -C_{TD}\rho_L K \nabla \in_L \tag{9}$$

where k and C_{TD} indicate the liquid TKE and turbulent dispersion coefficient. Various values of turbulent dispersion coefficient have been recommended in the previous studies [3, 15, 22, 37, 66]. In our simulation setting, turbulent dispersion coefficient of 0.3 is used based on the sensitivity study [3, 15, 37, 66]. The sensitivity study has been carried out for turbulent dispersion coefficients from 0.2 to 0.5 and the result shows a small difference in results of flow pattern and gas hold-up, while the value of 0.3 results in marginal improvement of flow pattern results.

In addition to interfacial forces, a proper selection of turbulence model is necessary to appropriately predict the bubble column hydrodynamics [3, 12-16, 22, 29, 37, 38, 66]. For the disperse bubbly phase a zero equation turbulence model is used. However, the standard k–ε model is applied for the continuous phase which have been used and recommended in prior CFD studies due to obtaining average results, simplicity and low computation time [3, 12-16, 22, 27-29, 37, 66, 68]. As k–ε is employed for turbulence modelling, the turbulent eddy viscosity is calculated using the standard k–ε turbulence model, where k represents the turbulent kinetic energy and ε its dissipation rate in the liquid phase. k and ε determine the energy in turbulence and the scale of the turbulence, respectively. The turbulent eddy viscosity can be defined as follows:

$$\mu_{T,L} = \rho_L C_\mu \frac{K^2}{\varepsilon} \tag{10}$$

The turbulent kinetic energy (k) and its energy dissipation rate (ε) are calculated based on the following governing equations:

$$\frac{\partial}{\partial t}(\rho_L \in_L K)+\nabla(\rho_L \in_L u_L K)=-\nabla(\in_L \frac{\mu_{eff,\mathrm{L}}}{\sigma_K}\nabla_K)+\in_L (G-\rho_L\varepsilon) \tag{11}$$

$$\frac{\partial}{\partial t}(\rho_L \in_L \varepsilon)+\nabla(\rho_L \in_L u_L\varepsilon)=-\nabla(\in_L \frac{\mu_{eff,\mathrm{L}}}{\sigma_\varepsilon}\nabla_\varepsilon)+\in_L \frac{\varepsilon}{K}(\mathrm{C}_{\varepsilon 1}G-\mathrm{C}_{\varepsilon 2}\rho_L\varepsilon) \tag{12}$$

Being k and ε calculated from their conservation equations. The k–ε model is applied, in this work, with its standard constants values (model parameters): $C_\mu = 0.09$, $\sigma_{k=}1, \sigma_\varepsilon = 1, C_{\varepsilon1} = 1.44, C_{\varepsilon2} = 1.92$. These constants, although not universal, are commonly used in the case of single-phase flow [19, 69]. The selection of these values based on recommendation of prior numerical studies [13, 15, 22, 37, 70]. The term G indicates the production of turbulent kinetic energy and can be represented as:

$$G=\tau_L : \nabla u_L \tag{13}$$

2.3.1 Grid

For meshing the cylindrical bubble column, the hexahedral grid is used throughout the column which is almost similar with study of Boutet et al. [71]. The circular cross section of bubble column is non-uniformly meshed, while the axial length of column is equally divided into 60 grids section. Fig. 2 shows a typical radial and axial grid layout for the 3D bubble column structure, containing 40500 grids. On average, this grid structure has the orthogonal quality of 0.67, skewness of 0.62 and aspect ratio of 3.1. In addition, two denser meshes (i.e., 59000 and 82320 elements) with similar structure are used for grid sensitivity study.

2.3.2 Boundary conditions

Instead of modelling the exact ring sparger for inlet condition, the mass source point is used for each sparger hole, calculating based on superficial gas velocity. At the top surface of the bubble column (outlet), a degassing boundary condition is treated, resulting in no penetration and slip condition for the liquid phase and an outlet for bubbles. In this case, the pressure remains variable on the top of the column, describing the various surface heights at different bubble column locations. On the walls, a no slip and free slip boundary conditions are used for the liquid and gas phases respectively. Considering the free slip boundary condition for the gas phase in Eulerian method describes the interaction between multi-bubbles and solid walls. As bubbles move towards the walls without fraction, they experience no interaction (freely movement) and the direct contacts between multi-bubbles and walls can be considered negligible. In this way, the velocity component parallel to the wall has a finite value, while both the velocity normal to the wall and the wall shear stress are set to zero.

2.3.3 Numerical methods

In order to mathematically discretize the conversation equations, the control volume technique is implemented throughout the 3D cylindrical bubble column. The velocity–pressure connection is achieved using SIMPLEC procedure. The high order differencing schemes of total variation diminishing (TVD) is used to decrease numerical diffusion in current CFD simulation study. The bubbling process is simulated for 1400s and the results are time averaged over last 1300s.

2.4 Adaptive-Network-based Fuzzy Inference System (ANFIS)

ANFIS is an inference fuzzy system to accurately predict the behavior of complex and nonlinear systems [40, 41, 47, 53, 54, 72]. There are three different types of fuzzy reasoning in which Takagi and Sugeno proposed if-then rules are implemented in ANFIS structure [73]. Fig. 3 shows the structure of the employed ANFIS method on predicting the hydrodynamic characteristics in the 3D bubble column. In this paper (three inputs, sparger diameter, radial coordination and axial coordination) are taken to obtain the gas hold up, TKE and axial liquid velocity as output (see Fig. 3). The inputs are divided into various numbers of membership functions (MFs) in first layer. The incoming signals from first layer are multiplied according to AND rule as the node function for the second layer. For instance, the function of the ith rule is as,

$$w_i = \mu_{A_i}\left(D_s\right)\times\mu_{B_i}\left(x\right)\times\mu_{C_i}\left(H\right) \quad (14)$$

where w_i is out coming signal of second layer's node and μ_{A_i}, μ_{B_i} and μ_{C_i} are incoming signals from implemented MFs on inputs, sparger diameter (D_s), axial coordination (H) and radial coordination (x), to second layer's node.

In layer three, the relative value of firing strength of each rule is calculated. This value equals to the weight of each layer over the total amount of all rules' firing strengths:

$$\bar{w}_i = \frac{w_i}{\sum_{i=1}^{n}\left(w_i\right)} \quad (15)$$

where $\bar{w}_i$ is called normalized firing strengths. The fourth layer applied the function of a consequence if-then rule proposed by Takagi and Sugeno [73]. Thus, the node function can be described as:

$$\bar{w}_i f_i = \bar{w}_i \left(p_i D_s + q_i x + r_i H + s_i \right)$$

where p_i, q_i, r_i and s_i are the if-then rules' parameters and called consequent parameters. All incoming signals from layer four are aggregated to obtain the model output represents the estimation result.

A hybrid learning algorithm is utilized to update the parameters in which MFs parameters are updated by gradient descent method and consequent parameters are updated by Least Square Estimate (LSE) method.

2.4.1 Membership function selection

One of the main aspects of this research is the investigation of the best type and number of MFs for all inputs in terms of the Root Mean Square Error (RMSE) and Correlation Coefficient (CC). The equation of RMSE can be defined as:

$$RMSE = \sqrt{\frac{1}{N}\sum_{i=1}^{N}(Actual\ Output - Estimated\ Output)^2} \tag{15}$$

where N is the number of testing sets.

The equation of CC that provides the relationship strength between prediction and CFD simulation results is as:

$$CC = \frac{\sum_{i=1}^{N}(y_{\mathrm{CFD}(i)} - y_{\mathrm{CFD}(m)})(y_{\mathrm{pre}(i)} - y_{\mathrm{pre}(m)})}{\sqrt{\sum_{i=1}^{N}(y_{\mathrm{CFD}(i)} - y_{\mathrm{CFD}(m)})^2 \sum_{i=1}^{N}(y_{\mathrm{pre}(i)} - y_{\mathrm{pre}(m)})^2}} \tag{16}$$

where $y_{CFD(i)}$ and $y_{CFD(m)}$ are the CFD result of individual data and the mean value of CFD results. $y_{pre(i)}$ and $y_{pre(m)}$ are the ANFIS prediction result of each data and the mean value of the prediction results.

In this aim, Bell-shaped, Gaussian and Sigmoidal MFs, and 27 combinations of number of MFs are employed to compare the estimation output errors. Table 1 portrays the equation of utilized MFs in the ANFIS model and Tables 2 and 3 depict the RMSE and CC values of various employed ANFIS structures.

Gaussian MF has two parameters (*c* and *σ*), Bell-shaped MF has three parameters (*a*, *b*, and *c*), and Sigmoidal MF has four parameters (a_1, a_2, c_1, and c_2). These parameters are called premise parameters. Numbers of MF are varied from 2 to 4 for each input and ANFIS structures are configured from 2-2-2 configuration, which means 2 MFs for sparger diameter (*Ds*), axial coordination (*H*) and radial coordination (*x*), to 4-4-4 configuration.

As seen in Tables 2 and 3, the most accurate ANFIS structures in terms of RMSE and CC values are 4-4-4 configuration with Sigmoidal MF for gas hold-up, 4-4-4 configuration with Bell-shaped MF for TKE and axial liquid velocity. Complexity of the model is another considerable parameter in selecting best ANFIS structure. In this aim, the total number of parameters, comprising premise and consequent parameters, is obtained for each model. This value is varied from 44 to 304 parameters.

Figs. 4, 6 and 8 portray gas hold-up, TKE and axial liquid velocity RMSE values of ANFIS structures in terms of number of parameters (premise and consequent) while Figs. 5, 7 and 9 show gas hold-up, TKE and axial liquid velocity CC values of ANFIS structures in terms of number of parameters. As seen in Fig. 4, RMSE results of gas hold-up illustrate an error reduction when the number of parameters increases. The RMSE results are distributed in two regions; high and low RMSE values. Different ANFIS configurations may have similar number of parameters which represents the complexity of the model.

As instance, ANFIS models with configuration of 2-3-4, 2-4-3, 3-2-4, 3-4-2, 4-2-3, and 4-3-2 have 114, 123, and 132 parameters for Gaussian, Bell-shaped, and Sigmoidal MFs, respectively. Type of MF has a slight influence on the gas hold-up prediction accuracy of gas hold-up while the number of parameters has a key role on the model precision. ANFIS models with configurations of 2-3-4, 2-4-3, 4-2-3, and 3-2-4 are much more accurate than models with configurations of 3-4-2 and 4-3-2. This comparison shows that radial coordination (*x*) needs to be split into more spaces by means of more MFs for *x*. Hence, ANFIS model with 4-4-4 configuration and Sigmoidal MF is selected as the best model to predict gas hold-up by comparing the RMSE and CC values and the influence of the ANFIS model configuration on the prediction accuracy.

Fig. 6 depicts the relationship between TKE RMSE values of diverse ANFIS models and numbers of parameters. In contrast with error result of gas hold-up prediction, TKE RMSE results are close together and reduction rate is lesser. Thus, a simpler ANFIS structure with less number of parameters can be chosen due to its simplicity and low RMSE value. ANFIS model with configuration of 4-4-4 has 280, 292, and 304 parameters for Gaussian, Bell-shaped, and Sigmoidal MFs while ANFIS model with configuration of 4-4-3 for Bell-shaped MF has 225 parameters. The RMSE values of these ANFIS models are close together. Therefore, the ANFIS model with lowest number of parameters can be selected as the best model to predict TKE. Fig. 7 illustrates that the ANFIS model with configuration of 4-4-3 and Bell-shaped MF has an appropriate performance in terms of CC value and is selected as the best ANFIS model for estimation of TKE.

Axial liquid velocity is another parameter that has been predicted by ANFIS method. Fig. 8 shows the RMSE values of diverse ANFIS structures versus number of parameters. As can be seen, the error result of utilizing Sigmoidal MF is higher than that of utilizing Bell-shaped and Gaussian MFs. The RMSE and CC results of ANFIS model with 2-4-4 configuration and Gaussian MF are close to those of models with higher complexity such as 3-4-4 configuration with Bell-shaped MF, 4-4-4 configuration with Gaussian and Bell-shaped MFs (see figs. 8 and 9). Hence, the best model in terms of both simplicity and accuracy is ANFIS model with 2-4-4 configuration and Gaussian MF to predict axial liquid velocity.

3 Results and discussion

3.1 Validation of CFD method

As the first step, it is important to establish the validity of the CFD model for prediction of the flow pattern and amount of gas inside the bubble column reactor. Therefore, a comparison has been made with the previous experimental and numerical data (i.e., Pfleger and Becker [13] and Diaz et al. [19]) and existing mathematical correlations (i.e., Joshi and Sharma [74], Kumar et al. [75], and Hughmark [76]). Excellent comparison is obtained between the current CFD estimation and previous studies for overall gas hold-up. For instance, Fig. 10 shows the overall gas hold-up against different superficial gas velocities for the present CFD simulation and previous studies. The overall gas hold-up inside the bubble column reactor linearly rises when the superficial gas velocity increases. This figure shows that the present finding of gas hold-up is in satisfactory agreement with experimental and numerical studies of Pfleger and Becker [13] (especially experimental finding) and Diaz et al. [19] and mathematical correlations of Joshi and Sharma [74] and Hughmark [76], when the superficial gas velocity alters from 0.0015m/s to 0.01m/s. However, the numerical study of Pfleger and Becker [13] overpredicts the gas hold-up almost for all superficial gas velocities.

Fig. 11 shows the planer averaged gas hold-up versus bubble column heights for Grids 1 and 3 and Pfleger and Becker's investigation [13]. In comparison to Pfleger and Becker's numerical study, current numerical results are in excellent agreement with experimental data, especially near the sparger. The Pfleger and Becker [13] showed an overprediction for gas hold-up at various column heights (particularly near the spargers). The figure shows that, towards the sparger, the numerical study of Pfleger and Becker [13] could not accurately estimate gas hold-up (over prediction), while the current CFD results are in good agreement with experimental data. In addition, the figure also illustrates that Grid 1 presents better agreement in comparison with Grid 3 in all column heights, particularly near the sparger.

3.2 Grid dependency

Three types of grids are used; Grid 1, Grid 2 and Grid 3 (mention in grid section), in order to investigate the effect of the mesh resolution on the results of flow pattern and amount of gas inside the bubble column.The CFD results of axial liquid velocity, based on three types of grids, are benchmarked against that from Pfleger and Becker experimental and numerical study [13]. Fig. 12 portrays the time averaged axial liquid velocity versus the normalized radial coordinate for Grids 1, 2, and 3 and experimental and numerical results of Pfleger and Becker at 1.6m column height. According to the figure, Grid 1 shows that axial flow is upward in the central region of column with higher gas hold-up, while a downward counter flow is observed towards the wall region with low gas hold-up. This hold-up gradient creates the density difference for liquid circulation to take place. The point of flow reversal is clearly seen at a radial location of around r/R = 0.6–0.8m. In contrast, the results of Grids 2 and 3 show the asymmetric liquid profile in which Grids 2 and 3 tend to move towards the right and left walls respectively. The results of Grid 1 also are in good agreement with numerical data of Pfleger and Becker [13].

In general, the grid dependency test shows a good agreement when the grid size increases (coarse mesh), while the numerical results with finer mesh differ more from experimental data of Pfleger and Becker [13] (see Figs. 11 and 12). Buwa et al. [69] and Pfleger and Becker [13] also reported that, as the grid size decreases, the agreement between numerical results of time averaged flow pattern and experimental finding deteriorates. Furthermore, Bech [77] showed that transient turbulence models produce new modes of instability in the plume oscillation when the grid size decreases. Based on results of grid dependency illustrated in Figs. 11 and 12, the coarse mesh, containing 40500 grids, is used for all simulation cases in this study.

3.3 Time step optimization

The influence of the time-step size on the flow pattern and gas hold-up results is also studied. In order to investigate the size of time step, the Courant–Friedrichs–Levy (CFL) number, is used. The CFL order number of one is necessary to resolve the transient bubbling process inside the column. The CFL number can be described as follows:

$$\Delta t \leq \frac{\Delta y}{|v|} \tag{17}$$

where $|v|$, Δy and Δt are the magnitude of the velocity vector's vertical component, characteristic dimension of the cell and time step, respectively. In order to study the effect of using different time steps on the accuracy of CFD results, time steps, ranging 0.1-0.01 are tested which results in small differences between results. In this study the time step of 0.1 is used for all CFD study. The selection of the time step is also evaluated by the CFL that the maximum CFL number must be less than one. Several investigations showed that when the CFL is smaller than 1, the numerical method can accurately predict the liquid flow pattern and gas dynamics and further refining of this parameter does not lead to significant changes on the results. However, using CFL larger than 1 results in inaccurate prediction results [17, 29, 38, 78-81].

3.4 Prediction evaluations and discussions

In this section, an accuracy evaluation and comparison between CFD and ANFIS results are discussed. Three different ANFIS models are proposed to predict the gas hold-up, TKE and axial liquid velocity individually. The results are divided into three portions: prediction evaluation, surface rules and mathematical models.

ANFIS model has been trained by using CFD simulation results. To verify the trained model, four axial coordinates, 0.867, 1.3, 1.733 and 2.167 m, are employed to examine the prediction result. Figs. 13-15 depict both CFD simulation and ANFIS prediction results for gas hold-up, TKE and axial liquid velocity in the bubble column. These figures illustrate the high capability of ANFIS method to model the characteristics of bubbly flow.

Inside bubble column reactors, the amount of gas depends upon the regime operation (i.e., homogeneous/heterogeneous) which turn depends upon column dimensions, pressure, temperature, superficial gas velocity and sparger design parameters. Fig. 13(a-d) shows gas hold–up results of CFD simulation and ANFIS prediction model at various bubble column heights (0.867, 1.3, 1.73 and 2.16 m) and sparger diameters (0.08m (Fig. 13(a)), 0.10m (Fig. 13(b)), 0.12 m (Fig. 13(c)) and 0.14 m (Fig. 13(d))). According to this figure, both CFD and ANFIS methods show that gas bubbles tend to move towards the bubble column center due to centralized gas movement in the homogeneous regime. An increase in sparger diameter from 0.08 to 0.14m causes a significant decrease in the magnitude of gas hold-up at the column center. Among all sparger diameters, the sparger diameter 0.14m produces almost flatter gas hold-up profile inside the bubble column reactor. Both CFD and ANFIS methods show that the gas hold-up profile is most likely uniform near the bubble column outlet. The figures show that ANFIS prediction method can estimate gas hold-up profile almost identical with CFD method towards the column center for various sparger diameters and bubble column heights.

Another important parameter in prediction of bubble column is TKE. When bubbles travel to the column surface, the pressure energy is converted to turbulent kinetic energy. This parameter shows the intensity of turbulence inside the bubble column reactor. Fig. 14 (a-d) compares CFD simulation and ANFIS prediction of TKE versus radial position in the column. According to the figure, TKE towards the column center is higher than other region, while near the wall region it reaches to zero due to higher fluctuations of turbulent fluid velocities at the column center. As the sparger diameter increases, TKE reduces particularly towards the column center. According to the figures, for all ring sparger diameters, TKE near the sparger region is much higher than bubble column outlet.

Axial liquid velocity is the last parameter that has been estimated by ANFIS approach. The ANFIS prediction result is compared with CFD simulation results in Fig. 15(a-d). As the sparger diameter rises, the liquid centerline velocity reduces and results in flatter liquid velocity profile. Additionally, the centerline liquid velocity decreases, as the column height increases. This is attributed to the fact that, near the sparger region, swarm bubbles supply higher energy to the liquid than bulk region, and resulting in higher turbulent dissipation energy. This energy transferring shows the critical bubble column location where bubble plume breaks and bubbles split to smaller bubbles (break-up). In summary, the results show that ANFIS approach beside the CFD method is a capable prediction methodology to estimate the local hydrodynamics parameters at various column locations and operation conditions.

This section provides information about 3D bubble column hydrodynamics surface plots in order to understand the flow pattern and gas dynamics throughout the bubble column for all column heights and sparger diameters. The predicted gas hold-up contour has been presented for various column heights and sparger diameters in Fig. 16. This figure shows the predicted gas hold-up for sparger diameters of 0.085m (16(a)), 0.115m (16(b)) and 0.145m (16(c)). According to the figure, the gas hold-up profile has a non-uniform behavior towards the sparger, while at the middle and surface region (e.g., 1.3 and 2.5m) gas phase disperses uniformly. In general, the gas hold-up has a maximum value at the central region while the amount of gas decreases as sparger diameter increases around this region (see Fig. 16). Fig. 17 portrays the predicted axial liquid velocity in different column heights and sparger diameters. As seen, maximum liquid velocity occurs near the sparger region at almost every column height, while the liquid direction changes and results in two recirculation area near walls. Fig. 18 depicts the predicted TKE for various column heights and sparger diameters (0.085m (18(a)), 0.115m (18(b)) and 0.145m (18(c))). According to this figure, TKE towards the sparger is significantly higher than other regions. The figure shows that, with an increase in sparger diameter, TKE decreases.

The ANFIS method can predict the BCR hydrodynamics with different operational conditions in less computational time and provide continuous results. In order to examine the prediction ability, the BCR hydrodynamics are predicted for different column heights. All predicted results are compared with CFD results which are not used in training process.

The ANFIS method is used to predict the results of ϵ_g at column heights (Y mesh coordinate) of 0.43, 0.86, 1.3, 1.73, 2.16 and 2.56 m. The number of prediction data in X and Z mesh coordinate is increased from 705 (CFD data) to 4800 nodes. For ANFIS training and model development, 70% of the actual data, which is the CFD results from benchmark case, at column heights of 0.217, 0.47, 0.73, 0.997, 1.3, 1.56, 1.8, 2.08, 2.3 and 2.6 m is given as an input. In addition, the number of data in X and Z mesh coordinate for the input is reduced to three quarter or to only 490 nodes. Please take note, the prediction is for the column heights that is not given as an input data to ANFIS model and hence the ability of the model is tested. Figure 19 shows the predicted contour plot of gas hold-up at various column heights (i.e., 0.432, 0.86, 1.3, 1.73, 2.17 and 2.56 m) for ANFIS and CFD method. According to the figure, the ANFIS results are in good agreement with CFD results almost for all column heights. The ANFIS method predicts the circular gas hold-up distribution almost for all column heights, which is similar with CFD results. Both CFD and ANFIS show the higher gas hold-up at the center region of column, ranging 0.02-0.03, while this parameter reaches to zero value near the walls. Towards the sparger region (h=0.432m), the sparger has influence on the gas distribution, resulting ring shape gas fraction (with 0.0012m inner and 0.09m outer diameter). As the column height increases, this influence diminishes and results in uniform distribution of gas. In comparison to CFD results, ANFIS method slightly over predicts the gas hold-up towards the walls at 2.56m. This may attribute to the fact that, ANFIS method cannot accurately recognize gas behaviour near the BCR boundary (particularly outlet). In order to enhance this over prediction, different ANFIS setting parameters or data filtering are required.

In summary, the combination of ANFIS and CFD prediction framework shows that, in case of a proper ANFIS learning process with CFD results, ANFIS approach can adequately predict bubble column hydrodynamics. In comparison to the CFD simulation, ANFIS approach provides the approximated bubble column hydrodynamics in a continuous domain. When the specific range of ring sparger diameters and column heights are trained in the ANFIS method, it can smartly approximate the flow pattern and gas dynamics within these particular ranges. On the other hand, in CFD simulation, the CFD simulation needs to be implemented for any changes in operation conditions due to production of discrete results. Therefore, providing a complete set of result for various conditions such as different sparger diameter requires computational efforts, resulting in large computational time.

In the last portion of this section, we propose the mathematical models of the liquid flow pattern and gas dynamics that have been estimated by selected ANFIS models. These mathematical correlations show the axial liquid velocity, gas hold-up and TKE at different column heights, radiuses and sparger diameters. The method of gaining mathematical models from ANFIS approach was described in section 2.4. The formula of the relationship between gas hold-up and effective variables, which are sparger diameter, axial coordination and radial coordination, can be written as,

$$\varepsilon_g = \frac{\sum_{i=1}^{4}\sum_{j=1}^{4}\sum_{k=1}^{4}\left(\mu_{1i}\times\mu_{2j}\times\mu_{3k}\right)\times\left(p_m D_s + q_m H + r_m x + s_m\right)}{\sum_{i=1}^{4}\sum_{j=1}^{4}\sum_{k=1}^{4}\left(\mu_{1i}\times\mu_{2j}\times\mu_{3k}\right)} \quad (18)$$

in which

$$\mu_{1i} = \frac{1}{1+e^{-a_{1i}\left(x-c_{1i}\right)}} - \frac{1}{1+e^{-a_{2i}\left(x-c_{2i}\right)}} \qquad \mu_{2j} = \frac{1}{1+e^{-a_{1j}\left(x-c_{1j}\right)}} - \frac{1}{1+e^{-a_{2j}\left(x-c_{2j}\right)}}$$

$$\mu_{3k} = \frac{1}{1+e^{-a_{1k}\left(x-c_{1k}\right)}} - \frac{1}{1+e^{-a_{2k}\left(x-c_{2k}\right)}}$$

First subscription of μ shows the input number and the second subscription depicts the MF number. The values of MFs' parameters (premise parameters) are shown in Table 4. Subscription of m represents the rule number ranged from 1 to 64. Table 5 shows the values of p_m, q_m, r_m, and s_m (consequent parameters). Each MF has four parameters and linear portion of every rule has four parameters. As seen in Table 4, the values of a_1 and a_2 for all MFs of individual input are approximately equal.

ANFIS model with 4-4-3 configuration and Bell-shaped MF is select among 81 ANFIS structures for prediction of turbulent kinetic energy. This model can be represented mathematically as,

$$TKE = \frac{\sum_{i=1}^{4}\sum_{j=1}^{4}\sum_{k=1}^{3}\left(\mu_{1i}\times\mu_{2j}\times\mu_{3k}\right)\times\left(p_m D_s + q_m H + r_m x + s_m\right)}{\sum_{i=1}^{4}\sum_{j=1}^{4}\sum_{k=1}^{3}\left(\mu_{1i}\times\mu_{2j}\times\mu_{3k}\right)} \quad (19)$$

in which

$$\mu_{1i} = \frac{1}{1+\left|\frac{x-c_i}{a_i}\right|^{2b_i}} \quad and \quad \mu_{1j} = \frac{1}{1+\left|\frac{x-c_j}{a_j}\right|^{2b_j}} \quad and \quad \mu_{1k} = \frac{1}{1+\left|\frac{x-c_k}{a_k}\right|^{2b_k}}$$

Table 6 depicts premise parameters and illustrates that the values of *b* for all MFs are pretty close to each other while *a* and *c* values are different. Forty-eight rules were constructed on the basis of the selected ANFIS structure and the values of p_m, q_m, r_m, and s_m parameters in these rules are portrayed in Table 7.

Axial liquid velocity is another element predicted by ANFIS approach. The selected ANFIS model to estimate the axial liquid velocity has the highest simplicity among chosen ANFIS models for prediction of gas hold-up and TKE. The equation of this model as follows:

$$V_y = \frac{\sum_{i=1}^{2}\sum_{j=1}^{4}\sum_{k=1}^{4}\left(\mu_{1i}\times\mu_{2j}\times\mu_{3k}\right)\times\left(p_m D_s + q_m H + r_m x + s_m\right)}{\sum_{i=1}^{2}\sum_{j=1}^{4}\sum_{k=1}^{4}\left(\mu_{1i}\times\mu_{2j}\times\mu_{3k}\right)} \quad (20)$$

in which

$$\mu_{1i} = e^{\frac{-\left(x-c_i\right)^2}{2\sigma_i^2}} \quad and \quad \mu_{1j} = e^{\frac{-\left(x-c_j\right)^2}{2\sigma_j^2}} \quad and \quad \mu_{1k} = e^{\frac{-\left(x-c_k\right)^2}{2\sigma_k^2}}$$

The values of premise and consequent parameters are shown in Tables 6 and 7. Overall, there are 20 premise parameters and 128 consequent parameters that have been refined by using CFD simulation axial liquid velocity results. Providing these types of mathematical models assists in improving the knowledge of flow pattern (flow field) and gas dynamics for various operation conditions. In addition, this model can predict much smarter when the number of trained data increases as input parameters (i.e., bubble column dimension in X, Y and Z direction, superficial gas velocity, gas and liquid properties).

4. Conclusions

This paper presents the combination of CFD and ANFIS to predict the 3D bubble column hydrodynamics for various ring sparger diameters at different bubble column heights. The Eulerian approach is used to simulate the liquid flow pattern and gas dynamics inside the 3D cylindrical bubble column reactor. The CFD simulation results are validated with existing numerical, experimental and mathematical correlations. After validation process, the CFD simulation results are used to train ANFIS approximation approach. The proper architectures of the ANFIS prediction models, in terms of number and type of MFs, are investigated to find the most accurate prediction model. Based on this model, the mathematical correlations for bubble column hydrodynamics are developed, as the sparger diameter and bubble column height change. The conclusions of this study are as follows:

- Both CFD and ANFIS prediction method show that the axial liquid velocity, turbulent kinetic energy and gas hold-up rise towards the column centre, while these parameters reach to zero value near the column walls for various gas sparger diameters and bubble column heights. The larger ring sparger diameter produces flatter gas hold-up profile in the bubble column cross-section. In addition, for all sparger diameters, the centreline velocity, gas hold-up and turbulent kinetic energy are higher near the sparger region.

- ANFIS approach can predict the bubble column hydrodynamics in a very short time and provide a non-discrete result, while the CFD simulation needs to be employed for any changes in operation condition.
- Evaluation of different ANFIS structures illustrates that the type and number of membership function significantly affect the precision of the prediction model.
- The ANFIS method contains a good ability to predict hydrodynamics parameters of bubble column reactor which are not used in the training process. This will show that, this method can be used as assistance tools together with CFD methodology to predict parameters and minimize computational efforts, and numerical repetition.

Acknowledgments

This research is financially supported by University of Malaya, Ministry of Higher Education High Impact Research (UM.C/HIR/MOHE/ENG/13) and the University of Malaya research grant (UMRG:RP031C-15AFR).

References

[1] N. Kantarci, F. Borak, K.O. Ulgen, Bubble column reactors, Process Biochemistry 40 (2005) 2263-2283.

[2] S. Mousavi, A. Jafari, S. Yaghmaei, M. Vossoughi, I. Turunen, Experiments and CFD simulation of ferrous biooxidation in a bubble column bioreactor, Computers & Chemical Engineering 32 (2008) 1681-1688.

[3] M. Pourtousi, J.N. Sahu, P. Ganesan, Effect of interfacial forces and turbulence models on predicting flow pattern inside the bubble column, Chemical Engineering and Processing: Process Intensification 75 (2014) 38-47.

[4] P. Zahedi, R. Saleh, R. Moreno-Atanasio, K. Yousefi, Influence of fluid properties on bubble formation, detachment, rising and collapse; Investigation using volume of fluid method, Korean Journal of Chemical Engineering 31 (2014) 1349-1361.

[5] R. Masood, Y. Khalid, A. Delgado, Scale adaptive simulation of bubble column flows, Chemical Engineering Journal 262 (2015) 1126-1136.

[6] R. Masood, A. Delgado, Numerical investigation of the interphase forces and turbulence closure in 3D square bubble columns, Chemical Engineering Science 108 (2014) 154-168.

[7] D.D. McClure, N. Aboudha, J.M. Kavanagh, D.F. Fletcher, G.W. Barton, Mixing in bubble column reactors: Experimental study and CFD modeling, Chemical Engineering Journal 264 (2015) 291-301.

[8] S. Şal, Ö.F. Gül, M. Özdemir, The effect of sparger geometry on gas holdup and regime transition points in a bubble column equipped with perforated plate spargers, Chemical Engineering and Processing: Process Intensification 70 (2013) 259-266.

[9] Y. Liu, O. Hinrichsen, Study on CFD–PBM turbulence closures based on k–ε and Reynolds stress models for heterogeneous bubble column flows, Computers & Fluids 105 (2014) 91-100.

[10] N.G. Deen, T. Solberg, B.H. Hjertager, Numerical simulation of the gas-liquid flow in a square cross-sectioned bubble column, 14th Int. Congress of Chemical and Process Engineering. Praha-Czech Republic, 2000.

[11] M. Dhotre, K. Ekambara, J. Joshi, CFD simulation of sparger design and height to diameter ratio on gas hold-up profiles in bubble column reactors, Experimental thermal and fluid science 28 (2004) 407-421.

[12] M. Dhotre, J. Joshi, Design of a gas distributor: Three-dimensional CFD simulation of a coupled system consisting of a gas chamber and a bubble column, Chemical Engineering Journal 125 (2007) 149-163.

[13] D. Pfleger, S. Becker, Modelling and simulation of the dynamic flow behaviour in a bubble column, Chemical Engineering Science 56 (2001) 1737-1747.

[14] D. Pfleger, S. Gomes, N. Gilbert, H.-G. Wagner, Hydrodynamic simulations of laboratory scale bubble columns fundamental studies of the Eulerian–Eulerian modelling approach, Chemical Engineering Science 54 (1999) 5091-5099.

[15] M.V. Tabib, S.A. Roy, J.B. Joshi, CFD simulation of bubble column—an analysis of interphase forces and turbulence models, Chemical Engineering Journal 139 (2008) 589-614.

[16] M. Dhotre, B. Niceno, B. Smith, Large eddy simulation of a bubble column using dynamic sub-grid scale model, Chemical Engineering Journal 136 (2008) 337-348.

[17] M.T. Dhotre, B. Niceno, B.L. Smith, M. Simiano, Large-eddy simulation (LES) of the large scale bubble plume, Chemical Engineering Science 64 (2009) 2692-2704.

[18] M.T. Dhotre, B.L. Smith, CFD simulation of large-scale bubble plumes: comparisons against experiments, Chemical Engineering Science 62 (2007) 6615-6630.

[19] M.E. Díaz, A. Iranzo, D. Cuadra, R. Barbero, F.J. Montes, M.A. Galán, Numerical simulation of the gas–liquid flow in a laboratory scale bubble column: influence of bubble size distribution and non-drag forces, Chemical Engineering Journal 139 (2008) 363-379.

[20] G. Besagni, G.R. Guédon, F. Inzoli, Annular Gap Bubble Column: Experimental Investigation and Computational Fluid Dynamics Modeling, Journal of Fluids Engineering 138 (2016) 011302.

[21] A. Gupta, S. Roy, Euler–Euler simulation of bubbly flow in a rectangular bubble column: Experimental validation with Radioactive Particle Tracking, Chemical Engineering Journal 225 (2013) 818-836.

[22] M.K. Silva, M.A. d'Ávila, M. Mori, Study of the interfacial forces and turbulence models in a bubble column, Computers & Chemical Engineering 44 (2012) 34-44.

[23] M. Sathe, J. Joshi, G. Evans, Characterization of turbulence in rectangular bubble column, Chemical Engineering Science 100 (2013) 52-68.

[24] A. Kulkarni, K. Ekambara, J. Joshi, On the development of flow pattern in a bubble column reactor: experiments and CFD, Chemical Engineering Science 62 (2007) 1049-1072.

[25] A.A. Kulkarni, Lift force on bubbles in a bubble column reactor: experimental analysis, Chemical Engineering Science 63 (2008) 1710-1723.

[26] A.A. Kulkarni, J.B. Joshi, Bubble formation and bubble rise velocity in gas-liquid systems: A review, Industrial & Engineering Chemistry Research 44 (2005) 5873-5931.

[27] P. Chen, Modeling the fluid dynamics of bubble column flows, Washington University, 2004. Department of Chemical Engineering., 2004.

[28] P. Chen, M. Duduković, J. Sanyal, Three‐dimensional simulation of bubble column flows with bubble coalescence and breakup, AIChE journal 51 (2005) 696-712.

[29] M. Dhotre, N. Deen, B. Niceno, Z. Khan, J. Joshi, Large eddy simulation for dispersed bubbly flows: a review, International Journal of Chemical Engineering 2013 (2013) 1-22.

[30] N.G. Deen, T. Solberg, B.H. Hjertager, Large eddy simulation of the gas–liquid flow in a square cross-sectioned bubble column, Chemical Engineering Science 56 (2001) 6341-6349.

[31] Q. Xiao, N. Yang, J. Li, Stability-constrained multi-fluid CFD models for gas–liquid flow in bubble columns, Chemical Engineering Science 100 (2013) 279-292.

[32] C. Xing, T. Wang, J. Wang, Experimental study and numerical simulation with a coupled CFD–PBM model of the effect of liquid viscosity in a bubble column, Chemical Engineering Science 95 (2013) 313-322.

[33] W. Li, W. Zhong, B. Jin, Y. Lu, T. He, Flow patterns and transitions in a rectangular three-phase bubble column, Powder Technology 260 (2014) 27-35.

[34] H. Wang, X. Jia, X. Wang, Z. Zhou, J. Wen, J. Zhang, CFD modeling of hydrodynamic characteristics of a gas–liquid two-phase stirred tank, Applied Mathematical Modelling 38 (2014) 63-92.

[35] S. Besbes, M. El Hajem, H.B. Aissia, J. Champagne, J. Jay, PIV measurements and Eulerian–Lagrangian simulations of the unsteady gas–liquid flow in a needle sparger rectangular bubble column, Chemical Engineering Science 126 (2015) 560-572.

[36] M.T. Islam, P. Ganesan, J. Cheng, A pair of bubbles' rising dynamics in a xanthan gum solution: a CFD study, RSC Advances 5 (2015) 7819-7831.

[37] M. Pourtousi, J.N. Sahu, P. Ganesan, S. Shamshirband, G. Redzwan, A combination of computational fluid dynamics (CFD) and adaptive neuro-fuzzy system (ANFIS) for prediction of the bubble column hydrodynamics, Powder Technology 274 (2015) 466-481.

[38] T. Ziegenhein, R. Rzehak, D. Lucas, Transient simulation for large scale flow in bubble columns, Chemical Engineering Science 122 (2015) 1-13.

[39] T. Ziegenhein, R. Rzehak, E. Krepper, D. Lucas, Numerical Simulation of Polydispersed Flow in Bubble Columns with the Inhomogeneous Multi‐Size‐Group Model, Chemie Ingenieur Technik 85 (2013) 1080-1091.

[40] A.M. Abdulshahed, A.P. Longstaff, S. Fletcher, The application of ANFIS prediction models for thermal error compensation on CNC machine tools, Applied Soft Computing 27 (2015) 158-168.

[41] C.S.N. Azwadi, M. Zeinali, A. Safdari, A. Kazemi, Adaptive-network-based fuzzy inference system analysis to predict the temperature and flow fields in a lid-driven cavity, Numerical Heat Transfer, Part A: Applications 63 (2013) 906-920.

[42] K. Chau, Application of a PSO-based neural network in analysis of outcomes of construction claims, Automation in Construction 16 (2007) 642-646.

[43] K. Chau, A split-step particle swarm optimization algorithm in river stage forecasting, Journal of hydrology 346 (2007) 131-135.

[44] K. Chau, Reliability and performance-based design by artificial neural network, Advances in Engineering Software 38 (2007) 145-149.

[45] K. Chau, F. Albermani, Knowledge-based system on optimum design of liquid retaining structures with genetic algorithms, Journal of structural engineering 129 (2003) 1312-1321.

[46] K. Chau, C. Cheng, Real-time prediction of water stage with artificial neural network approach, AI 2002: Advances in Artificial Intelligence, Springer2002, pp. 715-715.

[47] M. Kazemipoor, M. Hajifaraji, S. Shamshirband, D. Petković, M.L.M. Kiah, Appraisal of adaptive neuro-fuzzy computing technique for estimating anti-obesity properties of a medicinal plant, Computer methods and programs in biomedicine 118 (2015) 69-76.

[48] I. Inayat, S.S. Salim, S. Marczak, M. Daneva, S. Shamshirband, A systematic literature review on agile requirements engineering practices and challenges, Computers in human behavior 51 (2015) 915-929.

[49] S. Shamshirband, D. Petković, R. Hashim, S. Motamedi, N.B. Anuar, An appraisal of wind turbine wake models by adaptive neuro-fuzzy methodology, International Journal of Electrical Power & Energy Systems 63 (2014) 618-624.

[50] S. Shamshirband, D. Petković, R. Hashim, S. Motamedi, Adaptive neuro-fuzzy methodology for noise assessment of wind turbine, (2014).

[51] D. Petković, Ž. Ćojbašić, Adaptive neuro-fuzzy estimation of autonomic nervous system parameters effect on heart rate variability, Neural Computing and Applications 21 (2012) 2065-2070.

[52] D. Petković, Ž. Ćojbašić, S. Lukić, Adaptive neuro fuzzy selection of heart rate variability parameters affected by autonomic nervous system, Expert Systems with Applications 40 (2013) 4490-4495.

[53] D. Petković, M. Issa, N.D. Pavlović, N.T. Pavlović, L. Zentner, Adaptive neuro-fuzzy estimation of conductive silicone rubber mechanical properties, Expert Systems with Applications 39 (2012) 9477-9482.

[54] D. Petković, N.D. Pavlović, Ž. Ćojbašić, N.T. Pavlović, Adaptive neuro fuzzy estimation of underactuated robotic gripper contact forces, Expert systems with Applications 40 (2013) 281-286.

[55] M. Zeinali, S.A. Mazlan, A. Fatah, A. Yasser, H. Zamzuri, A GA-Weighted Adaptive Neuro-Fuzzy Model to Predict the Behaviour of Magnetorheological Damper, Applied Mechanics and Materials, Trans Tech Publ, 2014, pp. 203-207.

[56] M. Zeinali, S.A. Mazlan, A.Y.A. Fatah, H. Zamzuri, A phenomenological dynamic model of a magnetorheological damper using a neuro-fuzzy system, Smart Materials and Structures 22 (2013) 125013.

[57] A.M. Abdulshahed, A.P. Longstaff, S. Fletcher, A. Myers, Thermal error modelling of machine tools based on ANFIS with fuzzy c-means clustering using a thermal imaging camera, Applied Mathematical Modelling 39 (2015) 1837-1852.

[58] V. Nikolić, S. Shamshirband, D. Petković, K. Mohammadi, Ž. Ćojbašić, T.A. Altameem, A. Gani, Wind wake influence estimation on energy production of wind farm by adaptive neuro-fuzzy methodology, Energy 80 (2015) 361-372.

[59] K. Alhumaizi, Comparison of finite difference methods for the numerical simulation of reacting flow, Computers & chemical engineering 28 (2004) 1759-1769.

[60] C.N. Azwadi, M. Razzaghian, M. Pourtousi, A. Safdari, Numerical prediction of free convection in an open ended enclosure using lattice Boltzmann numerical method, Int. J. Mech. Mater. Eng 8 (2013) 58-62.

[61] M. Pourtousi, M. Razzaghian, A. Safdari, A.N. Darus, Simulation of fluid flow inside a back-ward-facing step by MRT-LBM, Int. Proc. Comput. Sci. Inf. Technol 33 (2012).

[62] M. Razzaghian, M. Pourtousi, A.N. Darus, Simulation of flow in lid driven cavity by MRT and SRT, International Conference on Mechanical and Robotics Engineering (ICMRE'2012) Phuket, 2012.

[63] A. Sheldareh, A. Safdari, M. Pourtousi, C. Sidik, N. Azwadi, Prediction of particle dynamics in lid-driven cavity flow, International Review on Modelling and Simulations 5 (2012) 1344-1347.

[64] Y. Sato, K. Sekoguchi, Liquid velocity distribution in two-phase bubble flow, International Journal of Multiphase Flow 2 (1975) 79-95.

[65] Y. Sato, M. Sadatomi, K. Sekoguchi, Momentum and heat transfer in two-phase bubble flow—I. Theory, International Journal of Multiphase Flow 7 (1981) 167-177.

[66] G. Li, X. Yang, G. Dai, CFD simulation of effects of the configuration of gas distributors on gas–liquid flow and mixing in a bubble column, Chemical Engineering Science 64 (2009) 5104-5116.

[67] M. Lopez de Bertodano, R. Lahey Jr, O. Jones, Turbulent bubbly two-phase flow data in a triangular duct, Nuclear engineering and design 146 (1994) 43-52.

[68] P. Chen, J. Sanyal, M. Duduković, Numerical simulation of bubble columns flows: effect of different breakup and coalescence closures, Chemical Engineering Science 60 (2005) 1085-1101.

[69] V.V. Buwa, V.V. Ranade, Dynamics of gas–liquid flow in a rectangular bubble column: experiments and single/multi-group CFD simulations, Chemical Engineering Science 57 (2002) 4715-4736.

[70] M. Elena Díaz, F.J. Montes, M.A. Galán, Influence of the lift force closures on the numerical simulation of bubble plumes in a rectangular bubble column, Chemical Engineering Science 64 (2009) 930-944.

[71] C. Laborde-Boutet, F. Larachi, N. Dromard, O. Delsart, D. Schweich, CFD simulation of bubble column flows: Investigations on turbulence models in RANS approach, Chemical Engineering Science 64 (2009) 4399-4413.

[72] M.T. Dastorani, Application of ANN and ANFIS Models on Dryland Precipitation Prediction (Case study: Yazd in central Iran, Journal of Applied Sciences 10 (2010).

[73] T. Takagi, M. Sugeno, Fuzzy identification of systems and its applications to modeling and control, Systems, Man and Cybernetics, IEEE Transactions on (1985) 116-132.

[74] J. Joshi, M. Sharma, A circulation cell model for bubble columns, Chemical Engineering Research and Design 57 (1979) 244-251.

[75] A. Kumar, T. Degaleesan, G. Laddha, H. Hoelscher, Bubble swarm characteristics in bubble columns, The Canadian Journal of Chemical Engineering 54 (1976) 503-508.

[76] G. Hughmark, Holdup and mass transfer in bubble columns, Industrial & Engineering Chemistry Process Design and Development 6 (1967) 218-220.

[77] K. Bech, Dynamic simulation of a 2D bubble column, Chemical engineering science 60 (2005) 5294-5304.

[78] T. Ma, D. Lucas, T. Ziegenhein, J. Fröhlich, N. Deen, Scale-Adaptive Simulation of a square cross-sectional bubble column, Chemical Engineering Science 131 (2015) 101-108.

[79] S. Laín, Dynamic three-dimensional simulation of gas-liquid flow in a cylindrical bubble column, Latin American applied research 39 (2009) 317-326.

[80] A. Buffo, D.L. Marchisio, M. Vanni, P. Renze, Simulation of polydisperse multiphase systems using population balances and example application to bubbly flows, Chemical Engineering Research and Design 91 (2013) 1859-1875.

[81] S. Laín, Large eddy simulation of gas-liquid flow in a bubble column reactor, El Hombre y la Máquina (2009) 108.

List of Tables:

Table 1 the equations of MFs used in the ANFIS model

Membership Function	Equation
Bell-shaped	$\dfrac{1}{1+\left\lvert\dfrac{x-c}{a}\right\rvert^{2b}}$
Gaussian	$e^{\frac{-(x-c)^2}{2\sigma^2}}$
Sigmoidal	$\dfrac{1}{1+e^{-a_1(x-c_1)}}-\dfrac{1}{1+e^{-a_2(x-c_2)}}$

Table 2 RMSE of utilized ANFIS structures

Number of MF			Output	RMSE for			Number of MF			Output	RMSE for		
D_s	H	x		Bell-Shaped MF	Gaussian MF	Sigmoidal MF	D_s	H	x		Bell-Shaped MF	Gaussian MF	Sigmoidal MF
			ϵ_g	0.0059	0.0060	0.0060				ϵ_g	0.0041	0.0042	0.0040
2	2	2	TKE	0.0025	0.0026	0.0030	3	3	4	TKE	0.0016	0.0017	0.0017
			V_y	0.0261	0.0263	0.0278				V_y	0.0131	0.0146	0.0162
			ϵ_g	0.0049	0.0049	0.0051				ϵ_g	0.0056	0.0057	0.0057
2	2	3	TKE	0.0021	0.0019	0.0022	3	4	2	TKE	0.0017	0.0021	0.0020
			V_y	0.0201	0.0207	0.0226				V_y	0.0189	0.0210	0.0225
			ϵ_g	0.0046	0.0048	0.0048				ϵ_g	0.0041	0.0043	0.0043
2	2	4	TKE	0.0022	0.0018	0.0022	3	4	3	TKE	0.0015	0.0016	0.0016
			V_y	0.0187	0.0182	0.0213				V_y	0.0131	0.0143	0.0174
			ϵ_g	0.0059	0.0060	0.0059				ϵ_g	0.0039	0.0038	0.0039
2	3	2	TKE	0.0022	0.0023	0.0024	3	4	4	TKE	0.0015	0.0015	0.0016
			V_y	0.0223	0.0237	0.0239				V_y	0.0111	0.0122	0.0137
			ϵ_g	0.0047	0.0048	0.0047				ϵ_g	0.0057	0.0058	0.0058
2	3	3	TKE	0.0019	0.0019	0.0018	4	2	2	TKE	0.0024	0.0026	0.0027
			V_y	0.0166	0.0178	0.0194				V_y	0.0255	0.0254	0.0265
			ϵ_g	0.0046	0.0046	0.0044				ϵ_g	0.0045	0.0047	0.0047
2	3	4	TKE	0.0019	0.0018	0.0018	4	2	3	TKE	0.0023	0.0023	0.0023
			V_y	0.0149	0.0152	0.0172				V_y	0.0192	0.0196	0.0216
			ϵ_g	0.0058	0.0059	0.0059				ϵ_g	0.0044	0.0045	0.0044
2	4	2	TKE	0.0020	0.0020	0.0026	4	2	4	TKE	0.0022	0.0018	0.0020
			V_y	0.0205	0.0222	0.0217				V_y	0.0168	0.0176	0.0198
			ϵ_g	0.0044	0.0045	0.0047				ϵ_g	0.0057	0.0057	0.0057
2	4	3	TKE	0.0017	0.0018	0.0018	4	3	2	TKE	0.0017	0.0020	0.0023
			V_y	0.0139	0.0163	0.0177				V_y	0.0218	0.0226	0.0225
			ϵ_g	0.0043	0.0044	0.0040				ϵ_g	0.0042	0.0045	0.0043
2	4	4	TKE	0.0017	0.0017	0.0018	4	3	3	TKE	0.0016	0.0017	0.0016
			V_y	0.0127	0.0109	0.0152				V_y	0.0153	0.0163	0.0180
			ϵ_g	0.0057	0.0058	0.0058				ϵ_g	0.0037	0.0040	0.0039
3	2	2	TKE	0.0024	0.0026	0.0029	4	3	4	TKE	0.0015	0.0016	0.0014
			V_y	0.0255	0.0255	0.0280				V_y	0.0124	0.0144	0.0148
			ϵ_g	0.0045	0.0047	0.0047				ϵ_g	0.0055	0.0057	0.0056
3	2	3	TKE	0.0024	0.0024	0.0020	4	4	2	TKE	0.0016	0.0018	0.0022
			V_y	0.0193	0.0196	0.0223				V_y	0.0204	0.0209	0.0203
			ϵ_g	0.0044	0.0044	0.0045				ϵ_g	0.0040	0.0043	0.0042
3	2	4	TKE	0.0024	0.0024	0.0019	4	4	3	TKE	0.0013	0.0015	0.0015
			V_y	0.0173	0.0179	0.0203				V_y	0.0130	0.0144	0.0163
			ϵ_g	0.0057	0.0058	0.0058				ϵ_g	0.0037	0.0034	0.0032
3	3	2	TKE	0.0018	0.0022	0.0021	4	4	4	TKE	0.0013	0.0013	0.0013
			V_y	0.0223	0.0224	0.0232				V_y	0.0094	0.0104	0.0127
			ϵ_g	0.0043	0.0044	0.0043							
3	3	3	TKE	0.0017	0.0019	0.0017							
			V_y	0.0157	0.0164	0.0189							

Table 3 CC of utilized ANFIS structures

Number of MF			Output	CC for			Number of MF			Output	CC for		
D_s	H	x		Bell-Shaped MF	Gaussian MF	Sigmoidal MF	D_s	H	x		Bell-Shaped MF	Gaussian MF	Sigmoidal MF
			ϵ_g	0.8997	0.8973	0.8984				ϵ_g	0.9524	0.9499	0.9552
2	2	2	TKE	0.9598	0.9414	0.9124	3	3	4	TKE	0.9845	0.9776	0.9838
			V_y	0.9272	0.9265	0.9171				V_y	0.9821	0.9778	0.9728
			ϵ_g	0.9331	0.9311	0.9282				ϵ_g	0.9110	0.9063	0.9088
2	2	3	TKE	0.9771	0.9499	0.9750	3	4	2	TKE	0.9767	0.9653	0.9639
			V_y	0.9576	0.9548	0.9459				V_y	0.9627	0.9536	0.9465
			ϵ_g	0.9399	0.9357	0.9342				ϵ_g	0.9531	0.9487	0.9486
2	2	4	TKE	0.9775	0.9505	0.9752	3	4	3	TKE	0.9840	0.9831	0.9830
			V_y	0.9635	0.9655	0.9522				V_y	0.9823	0.9786	0.9682
			ϵ_g	0.9008	0.8982	0.8993				ϵ_g	0.9582	0.9601	0.9572
2	3	2	TKE	0.9704	0.9673	0.9533	3	4	4	TKE	0.9850	0.9826	0.9852
			V_y	0.9473	0.9406	0.9398				V_y	0.9874	0.9847	0.9804
			ϵ_g	0.9379	0.9347	0.9373				ϵ_g	0.9080	0.9047	0.9043
2	3	3	TKE	0.9798	0.9800	0.9770	4	2	2	TKE	0.9596	0.9237	0.9309
			V_y	0.9711	0.9669	0.9605				V_y	0.9310	0.9315	0.9252
			ϵ_g	0.9413	0.9404	0.9460				ϵ_g	0.9422	0.9378	0.9386
2	3	4	TKE	0.9813	0.9798	0.9796	4	2	3	TKE	0.9422	0.9401	0.9339
			V_y	0.9770	0.9759	0.9691				V_y	0.9616	0.9599	0.9507
			ϵ_g	0.9025	0.8997	0.9016				ϵ_g	0.9459	0.9437	0.9455
2	4	2	TKE	0.9749	0.9680	0.9586	4	2	4	TKE	0.9780	0.9490	0.9441
			V_y	0.9558	0.9480	0.9504				V_y	0.9707	0.9677	0.9589
			ϵ_g	0.9460	0.9432	0.9386				ϵ_g	0.9081	0.9092	0.9064
2	4	3	TKE	0.9811	0.9803	0.9783	4	3	2	TKE	0.9772	0.9740	0.9424
			V_y	0.9798	0.9724	0.9672				V_y	0.9498	0.9462	0.9465
			ϵ_g	0.9493	0.9465	0.9556				ϵ_g	0.9511	0.9430	0.9491
2	4	4	TKE	0.9822	0.9814	0.9801	4	3	3	TKE	0.9843	0.9812	0.9818
			V_y	0.9832	0.9877	0.9760				V_y	0.9757	0.9723	0.9660
			ϵ_g	0.9067	0.9026	0.9037				ϵ_g	0.9611	0.9547	0.9573
3	2	2	TKE	0.9537	0.9217	0.9281	4	3	4	TKE	0.9915	0.9832	0.9900
			V_y	0.9306	0.9308	0.9157				V_y	0.9840	0.9785	0.9774
			ϵ_g	0.9422	0.9374	0.9372				ϵ_g	0.9126	0.9080	0.9096
3	2	3	TKE	0.9651	0.9499	0.9762	4	4	2	TKE	0.9802	0.9708	0.9475
			V_y	0.9611	0.9596	0.9477				V_y	0.9564	0.9542	0.9567
			ϵ_g	0.9457	0.9447	0.9440				ϵ_g	0.9553	0.9489	0.9508
3	2	4	TKE	0.9440	0.9463	0.9824	4	4	3	TKE	0.9917	0.9893	0.9870
			V_y	0.9687	0.9664	0.9568				V_y	0.9824	0.9786	0.9722
			ϵ_g	0.9082	0.9035	0.9056				ϵ_g	0.9612	0.9687	0.9717
3	3	2	TKE	0.9695	0.9574	0.9601	4	4	4	TKE	0.9936	0.9930	0.9915
			V_y	0.9476	0.9470	0.9433				V_y	0.9909	0.9888	0.9834
			ϵ_g	0.9494	0.9470	0.9473							
3	3	3	TKE	0.9824	0.9791	0.9816							
			V_y	0.9742	0.9720	0.9625							

Table 4 Premise parameters of gas hold-up's ANFIS prediction model

Input	MF	a_1	c_1	a_2	c_2
Sparger Diameter	1	4.444e+02	5.495e-02	4.444e+02	7.955e-02
	2	4.444e+02	9.655e-02	4.444e+02	1.161e-01
	3	4.444e+02	1.067e-01	4.444e+02	1.333e-01
	4	4.444e+02	1.571e-01	4.444e+02	1.750e-01
Axial Coordination	1	1.538e+01	-4.332e-01	1.539e+01	-6.853e-02
	2	1.539e+01	1.943e-01	1.538e+01	1.286e+00
	3	1.538e+01	1.197e+00	1.538e+01	2.172e+00
	4	1.538e+01	2.160e+00	1.538e+01	3.033e+00
Radial Coordination	1	1.390e+02	-1.919e-01	1.390e+02	-4.025e-02
	2	1.390e+02	-5.078e-02	1.390e+02	3.719e-02
	3	1.390e+02	3.270e-02	1.390e+02	6.373e-02
	4	1.390e+02	5.365e-02	1.390e+02	1.918e-01

Table 5 Consequent parameters of gas hold-up's ANFIS prediction model

Rule	*p*	*q*	*r*	*s*	Rule	*p*	*q*	*r*	*s*
1	2.06e-01	-9.83e-02	-3.13e-01	-4.81e-02	33	3.82e-01	2.60e-01	8.93e-01	4.96e-02
2	-5.34e-01	1.29e+00	-1.77e+00	4.37e-02	34	-6.72e-01	-1.27e-02	6.73e-01	8.78e-02
3	1.55e+00	8.96e-01	-1.35e+01	6.23e-01	35	-1.65e+00	8.76e-01	6.47e+00	-5.24e-02
4	-5.06e-01	-1.17e-01	-4.00e-01	9.51e-02	36	2.24e-01	2.53e-02	1.13e-01	-4.47e-02
5	-5.94e-01	3.96e-03	1.23e-01	5.75e-02	37	-2.40e-02	1.98e-03	3.64e-01	4.88e-02
6	-3.63e-01	7.86e-03	3.59e-01	7.16e-02	38	-4.16e-01	-1.05e-02	8.52e-02	9.34e-02
7	2.50e+00	2.43e-02	6.92e-01	-1.90e-01	39	8.82e-01	6.61e-03	1.75e-01	-9.68e-02
8	-6.96e-02	8.56e-03	-1.13e-01	1.52e-02	40	-1.48e-01	5.68e-03	-2.07e-01	4.29e-02
9	-3.33e-01	3.06e-03	2.04e-01	4.73e-02	41	-9.09e-02	1.57e-03	2.63e-01	4.72e-02
10	5.32e-01	-5.28e-03	1.87e-01	1.17e-02	42	-2.72e-01	-4.60e-03	3.95e-02	7.16e-02
11	1.43e+00	3.94e-03	3.02e-01	-9.52e-02	43	2.12e-01	-7.98e-04	7.83e-02	-5.00e-03
12	2.25e-01	4.51e-03	-2.32e-01	8.20e-03	44	2.08e-02	3.11e-03	-2.27e-01	2.46e-02
13	-2.26e-01	9.50e-03	2.00e-01	2.31e-02	45	-3.84e-02	5.75e-03	2.29e-01	2.65e-02
14	2.48e-01	3.12e-03	1.37e-01	1.05e-02	46	-2.20e-01	-5.82e-03	5.25e-02	6.97e-02
15	9.01e-01	-3.44e-03	2.06e-01	-3.86e-02	47	9.88e-02	3.85e-03	5.65e-02	-1.62e-03
16	1.43e-01	5.88e-03	-2.23e-01	8.75e-03	48	4.17e-02	6.62e-03	-2.09e-01	1.09e-02
17	5.02e-01	1.48e-02	4.36e-02	-4.27e-02	49	-6.29e-02	2.26e-01	9.12e-01	1.15e-01
18	-1.14e+00	6.72e-01	-1.65e+00	9.57e-02	50	-3.45e-01	8.55e-02	6.66e-01	3.97e-02
19	-2.40e+00	4.16e-01	-1.50e+00	4.44e-01	51	-4.37e-01	-5.38e-02	-5.82e-01	5.43e-02
20	2.88e-01	1.11e-02	3.96e-01	-7.65e-02	52	-3.72e-02	1.73e-01	-9.34e-01	1.23e-01
21	-1.99e-01	5.30e-03	2.05e-01	4.28e-02	53	1.17e-02	5.71e-03	3.95e-01	4.61e-02
22	-6.42e-01	-4.30e-03	1.13e-01	1.10e-01	54	-5.77e-01	-1.10e-02	-1.41e-01	1.14e-01
23	9.91e-01	6.76e-03	7.56e-01	-1.05e-01	55	-1.13e+00	-3.36e-03	-2.71e-02	2.05e-01
24	6.10e-03	7.05e-04	-1.77e-01	2.19e-02	56	3.13e-01	6.17e-04	-3.96e-01	3.84e-03
25	-2.00e-01	2.86e-03	2.33e-01	4.68e-02	57	6.16e-02	2.01e-03	2.95e-01	3.02e-02
26	-1.51e-01	-6.19e-03	6.05e-02	6.00e-02	58	-3.37e-01	-2.57e-03	-4.69e-02	7.39e-02
27	4.69e-01	-2.02e-04	1.72e-01	-2.64e-02	59	-2.38e-01	-3.14e-03	-1.39e-01	7.15e-02
28	8.65e-02	1.51e-03	-2.22e-01	2.04e-02	60	1.64e-01	1.06e-03	-2.82e-01	1.50e-02
29	-1.21e-01	6.74e-03	2.17e-01	2.77e-02	61	6.03e-02	5.18e-03	2.35e-01	1.60e-02
30	-1.56e-01	1.43e-03	5.58e-02	4.38e-02	62	-2.50e-01	-6.52e-03	-2.41e-02	7.24e-02
31	2.01e-01	5.99e-03	1.40e-01	-1.50e-02	63	-1.22e-01	-5.83e-03	-1.27e-01	5.98e-02
32	4.97e-02	4.99e-03	-2.05e-01	1.43e-02	64	1.08E-01	4.57E-03	-2.37E-01	1.05E-02

Table 6 Premise parameters of turbulent kinetic energy's ANFIS prediction model

Input	MF	*a*	*b*	*c*
Sparger Diameter	1	3.393e-03	2.000e+00	8.292e-02
	2	6.082e-03	2.001e+00	1.227e-01
	3	1.200e-02	2.000e+00	1.804e-01
	4	3.643e-03	2.000e+00	1.551e-01
Axial Coordination	1	4.189e-01	1.996e+00	-2.915e-02
	2	4.684e-01	2.001e+00	8.275e-01
	3	4.452e-01	2.000e+00	1.731e+00
	4	4.316e-01	2.000e+00	2.604e+00
Radial Coordination	1	1.028e-01	2.000e+00	-1.210e-01
	2	1.036e-01	1.999e+00	9.861e-03
	3	1.078e-01	1.999e+00	1.299e-01

Table 7 Consequent parameters of turbulent kinetic energy's ANFIS prediction model

Rule	*p*	*q*	*r*	*s*	Rule	*p*	*q*	*r*	*s*
1	2.80e-01	-1.33e-02	6.51e-02	-1.84e-02	25	-1.19e+00	-1.45e-01	-7.61e-01	5.80e-02
2	-4.17e-01	1.94e-01	-1.85e-01	2.40e-02	26	2.03e+00	7.35e-02	-6.50e-01	-2.77e-01
3	1.07e-01	-4.24e-02	-2.82e-01	4.06e-02	27	-8.98e-01	6.99e-02	-7.17e-01	2.47e-01
4	1.60e-01	2.09e-04	6.26e-01	8.82e-02	28	-1.18e+00	-2.83e-03	-1.10e-01	1.56e-01
5	-8.39e-02	2.38e-03	3.88e-01	4.28e-04	29	-2.52e+00	1.10e-02	-1.51e-01	3.12e-01
6	-1.53e-01	-5.04e-03	-2.20e-01	3.61e-02	30	1.79e+00	-7.02e-03	-1.02e+00	-8.78e-02
7	7.07e-02	-1.14e-03	5.45e-01	8.36e-02	31	-1.05e-01	2.31e-03	1.94e-01	5.19e-02
8	2.65e-01	2.77e-03	2.38e-01	-3.78e-02	32	-3.10e+00	1.05e-02	4.82e-01	4.13e-01
9	-2.50e-01	-4.47e-03	-2.82e-01	6.38e-02	33	1.11e+00	-1.03e-02	-2.47e-01	-1.15e-01
10	-1.36e-02	-6.68e-04	3.57e-01	6.19e-02	34	1.80e-01	1.41e-02	1.36e-01	-3.22e-02
11	-2.73e-02	-1.92e-03	1.88e-01	3.26e-03	35	-6.42e-01	1.17e-02	1.98e-01	6.21e-02
12	-5.67e-02	7.82e-03	-1.84e-01	7.49e-03	36	8.92e-02	-2.20e-02	-1.53e-01	5.87e-02
13	1.78e-01	6.15e-03	3.50e-01	3.15e-02	37	8.98e-01	5.27e-02	6.83e-01	-3.04e-02
14	-7.65e-02	1.20e-01	1.18e-01	-1.25e-02	38	-1.75e+00	5.31e-02	3.79e-01	2.31e-01
15	3.50e-02	-1.32e-02	-2.33e-01	2.75e-02	39	1.27e+00	-1.36e-02	-1.27e-01	-1.84e-01
16	1.65e-01	-1.60e-03	7.61e-01	1.04e-01	40	9.84e-01	-4.15e-03	9.44e-01	1.32e-02
17	-2.55e-01	3.30e-03	3.92e-01	-3.91e-04	41	1.59e+00	3.29e-03	5.41e-01	-2.92e-01
18	9.51e-03	-3.17e-03	-3.84e-01	4.86e-02	42	-1.44e+00	-9.89e-03	-3.76e-01	2.67e-01
19	7.87e-02	-1.26e-03	5.14e-01	7.51e-02	43	9.84e-02	-3.64e-03	4.83e-01	7.11e-02
20	-1.78e-01	-2.31e-03	1.73e-01	3.81e-03	44	2.00e+00	9.41e-04	1.84e-01	-3.23e-01
21	-6.91e-02	-6.62e-04	-3.70e-01	6.18e-02	45	-9.52e-01	-4.91e-03	-2.55e-01	1.87e-01
22	2.01e-02	-2.73e-03	3.56e-01	6.24e-02	46	-3.14e-01	-1.11e-02	3.23e-01	1.28e-01
23	-2.22e-01	-1.68e-03	1.36e-01	1.70e-02	47	1.22e-01	9.00e-03	1.33e-01	-5.63e-02
24	3.18e-02	-1.55e-03	-2.62e-01	3.70e-02	48	6.67e-02	-5.35e-03	-1.83e-01	2.88e-02

833 **Table 8** Premise parameters of axial liquid velocity's ANFIS prediction model

Input	MF	σ	c
Sparger Diameter	1	3.107e-02	8.611e-02
	2	1.996e-02	1.526e-01
Axial Coordination	1	2.215e-01	-1.589e-01
	2	4.978e-01	8.053e-01
	3	4.685e-01	1.798e+00
	4	9.646e-02	2.793e+00
Radial Coordination	1	5.538e-03	-1.434e-01
	2	8.356e-02	-7.177e-02
	3	6.069e-02	4.728e-02
	4	9.647e-02	3.347e-01

Table 9 Consequent parameters of axial liquid velocity's ANFIS prediction model

rule	p	q	r	s	rule	p	q	r	s
1	7.86e-01	-2.80e-02	5.72e+00	7.48e-01	17	4.05e+00	-2.13e-01	-7.61e+00	-1.70e+00
2	-1.31e+00	-2.58e-02	-9.81e-01	-1.61e-02	18	-6.29e+00	2.47e-01	1.38e-01	9.77e-01
3	5.63e-01	3.97e-01	-1.06e+00	2.45e-02	19	6.33e+00	1.36e-03	8.17e-01	-1.04e+00
4	1.44e+00	-1.61e+00	-1.14e+01	1.80e+00	20	-3.41e+00	-2.88e-01	-2.54e+00	8.45e-01
5	5.01e-02	-1.27e-02	-5.08e+00	-6.45e-01	21	1.01e+00	-8.13e-03	-4.67e+00	-6.91e-01
6	-3.00e-02	1.28e-02	1.71e+00	1.16e-01	22	-1.41e+00	1.74e-02	4.10e+00	6.10e-01
7	1.17e-01	7.43e-03	-2.49e+00	2.31e-01	23	1.46e+00	-2.23e-03	2.36e+00	-3.01e-01
8	1.71e+00	-7.45e-02	2.01e+01	-2.85e+00	24	2.63e+00	1.01e-01	7.99e+01	-1.27e+01
9	-6.69e-02	-7.13e-03	-1.14e+01	-1.54e+00	25	5.03e-01	-1.76e-03	-1.08e+01	-1.53e+00
10	1.34e-01	6.32e-03	1.89e+00	1.33e-01	26	-6.83e-01	5.31e-03	2.87e+00	3.74e-01
11	-1.31e-01	-3.75e-03	-1.18e+00	1.71e-01	27	5.11e-01	3.22e-03	1.15e+00	-9.72e-02
12	1.13e+00	-2.02e-02	2.77e+01	-4.11e+00	28	2.05e+00	4.98e-02	5.42e+01	-8.72e+00
13	3.08e-01	1.54e+00	6.78e+00	-3.15e+00	29	-1.40e+00	5.06e-01	7.71e+00	-1.30e-01
14	-1.05e-01	-1.78e+00	-2.62e+00	4.44e+00	30	1.50e+00	-4.56e-01	-3.53e+00	6.58e-01
15	-1.95e-01	-2.42e+00	2.93e+00	6.00e+00	31	-2.47e+00	1.35e-01	2.20e+00	-1.69e-01
16	-4.68e-01	1.01e+01	-2.75e+01	-2.23e+01	32	-1.12E+00	-6.44E-01	-3.55E+01	6.94E+00

Figures

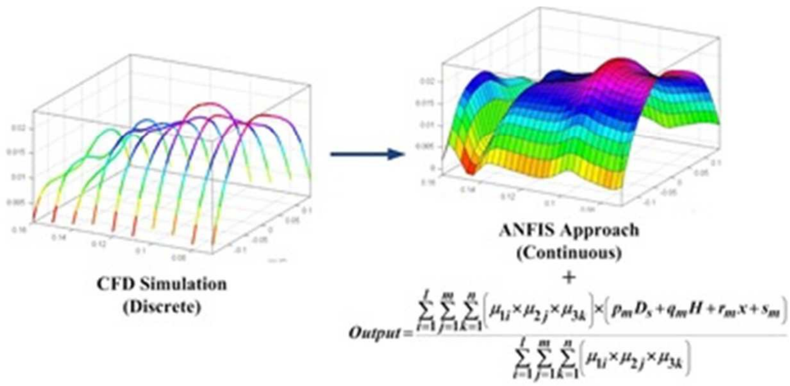

Figure 1 Schematic of prediction procedure of bubble column using the combination of CFD and ANFIS.

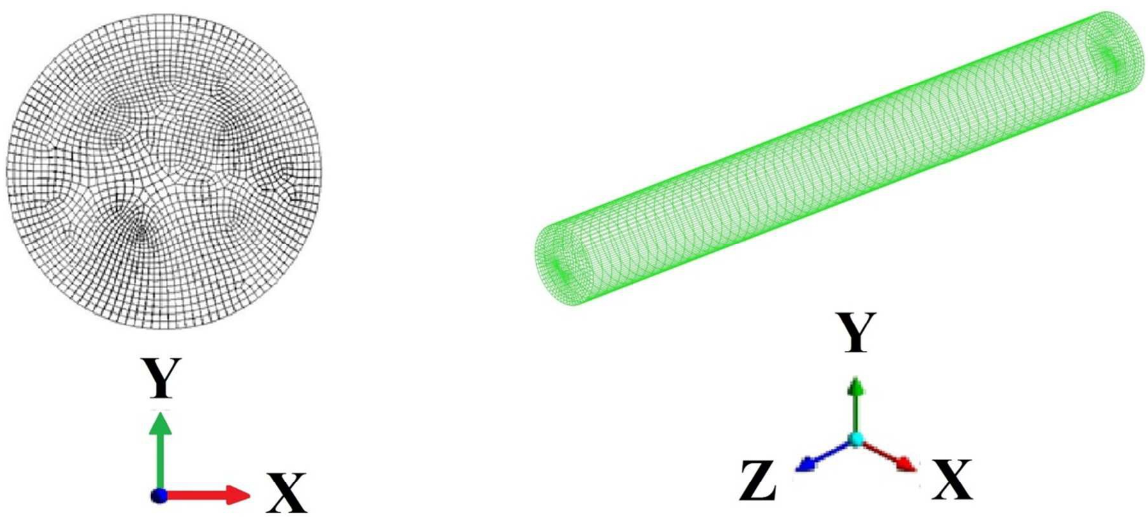

Figure 2 Grid intensity of the present CFD study containing 40500 structural elements.

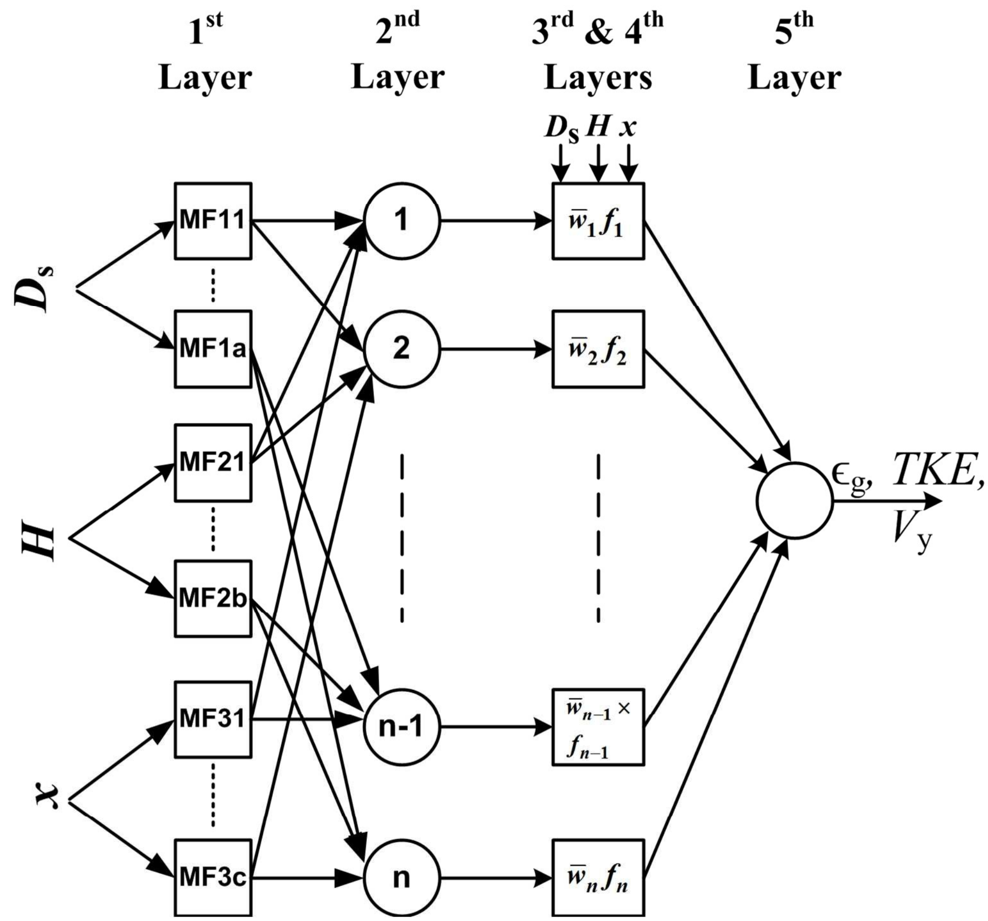

Figure 3 Schematic of the ANFIS structure

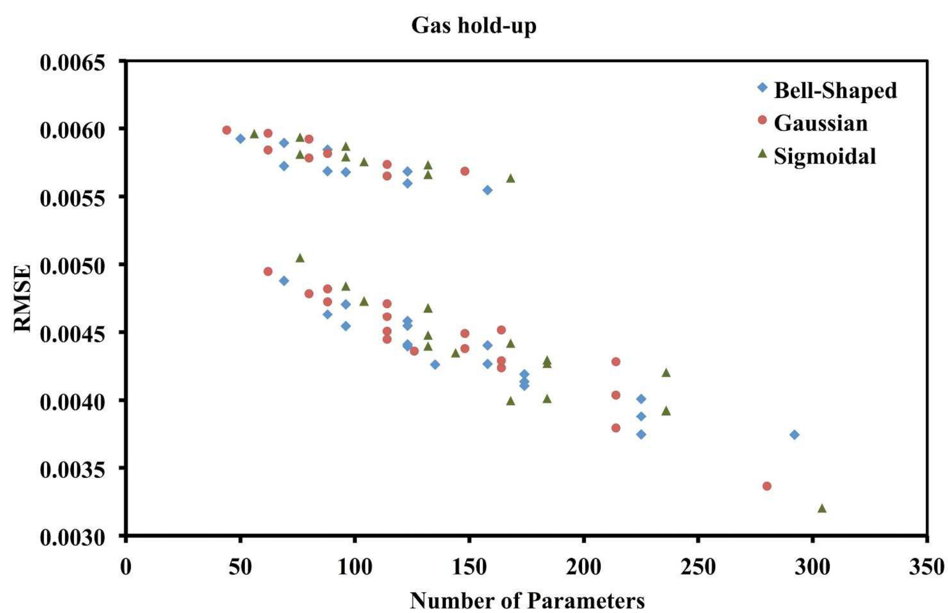

Figure 4 Gas hold-up RMSE values of ANFIS methods versus number of parameters.

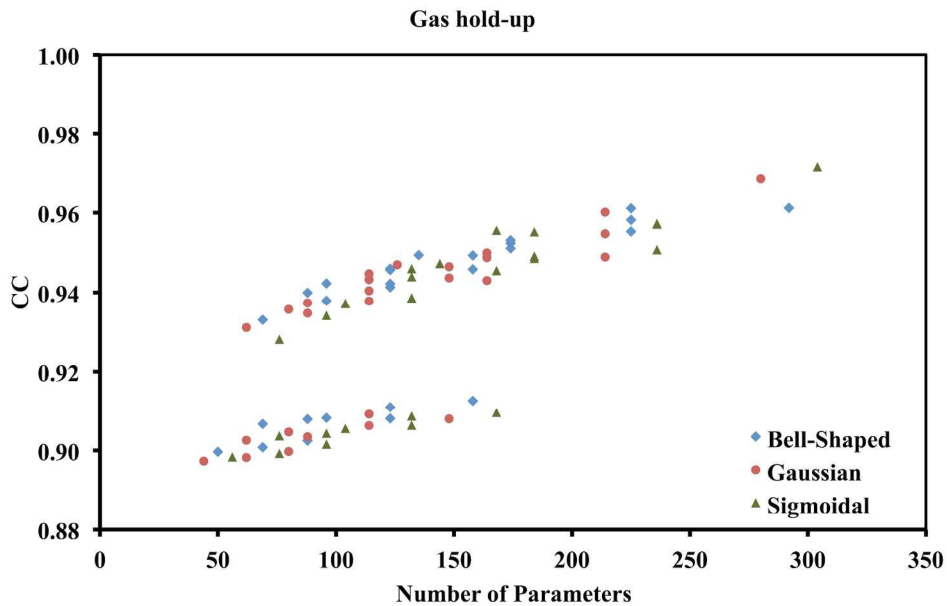

Figure 5 Gas hold-up CC of ANFIS methods versus number of parameters.

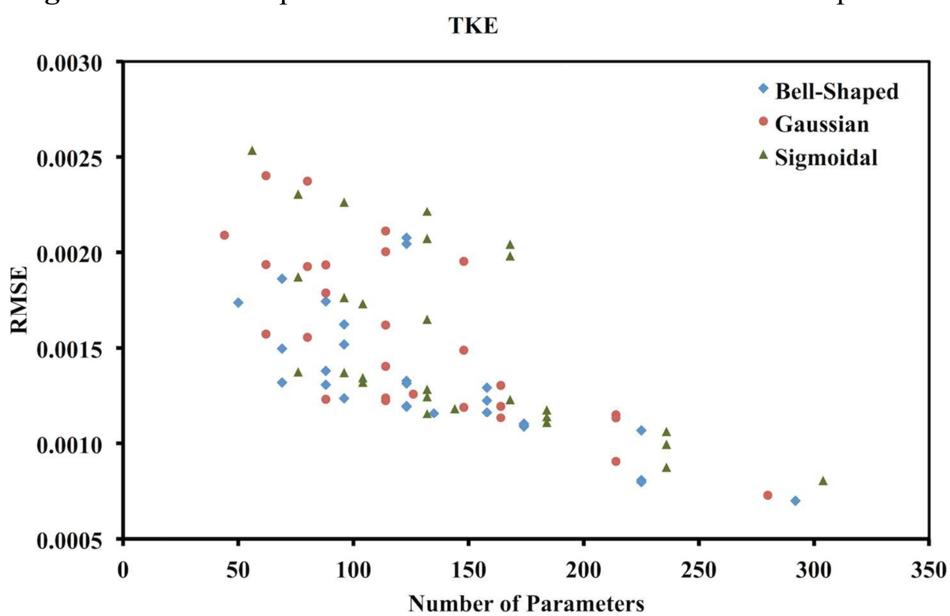

Figure 6 TKE RMSE values of ANFIS methods versus number of parameters.

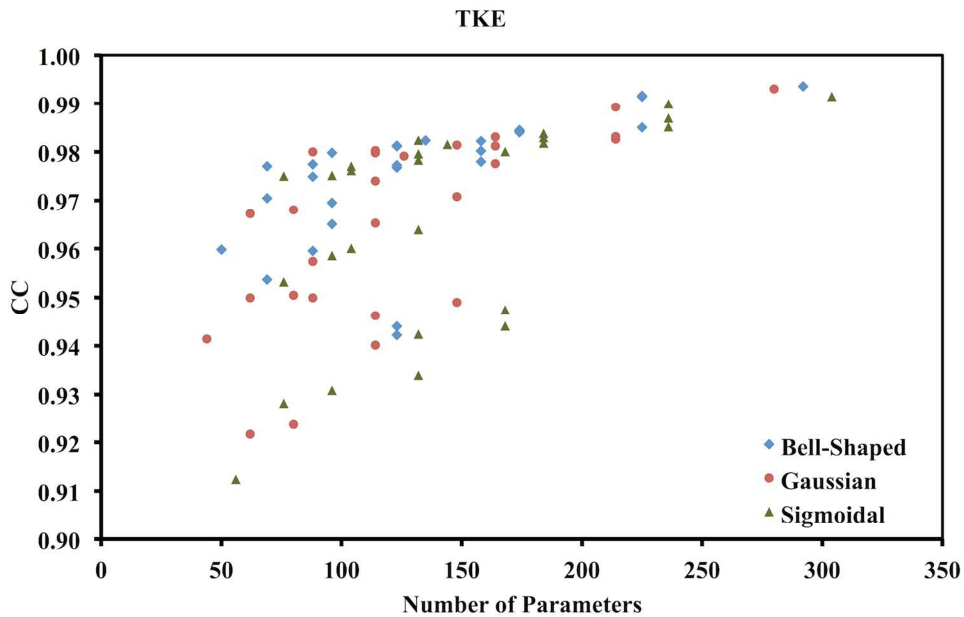

Figure 7 TKE CC of ANFIS methods versus number of parameters.

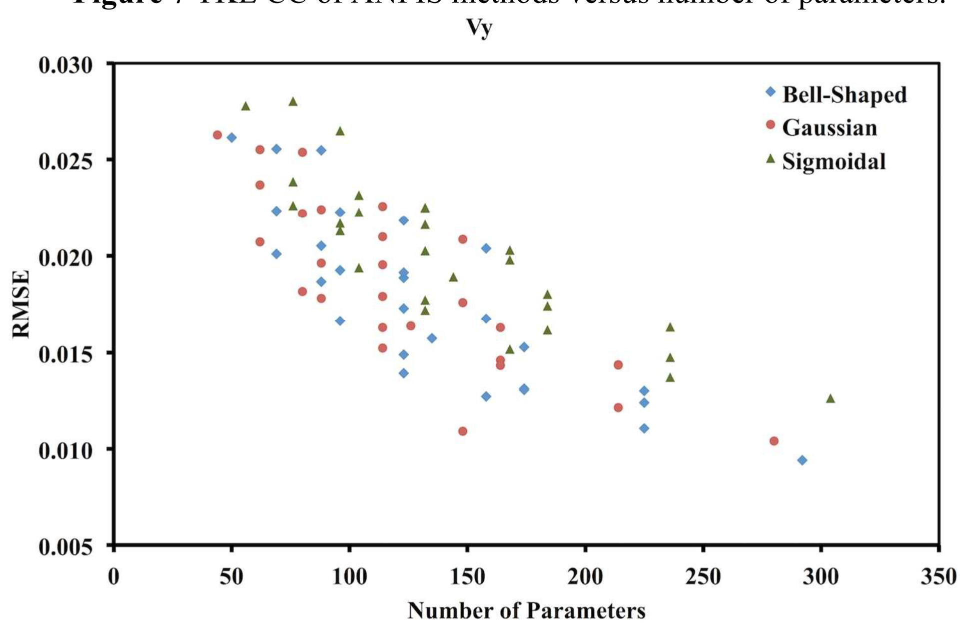

Figure 8 Axial velocity RMSE values of ANFIS methods versus number of parameters.

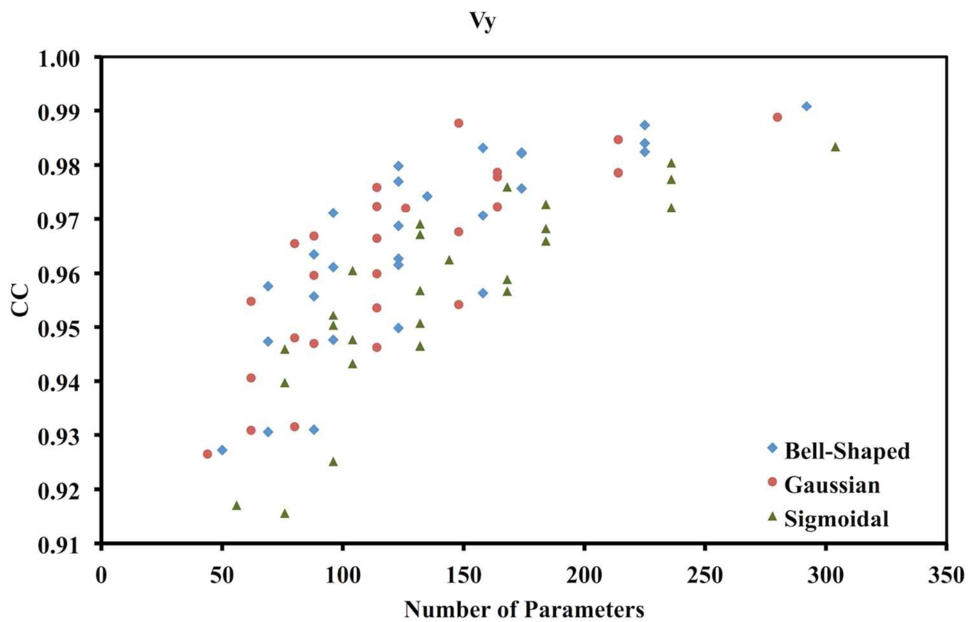

Figure 9 Axial velocity CC of ANFIS methods versus number of parameters.

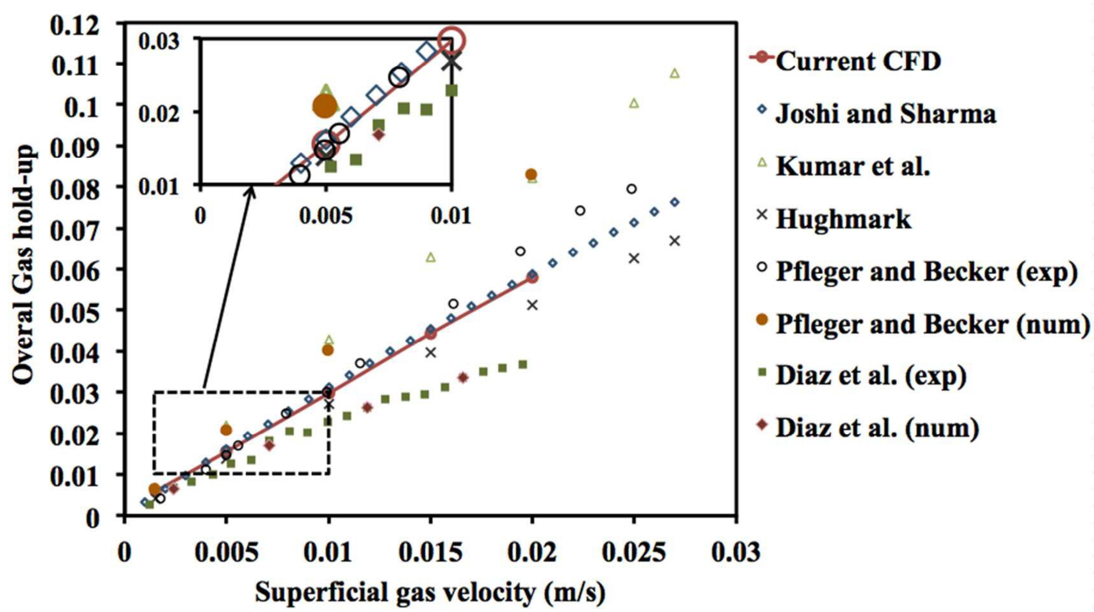

Figure 10 Overall gas hold up for current simulation.

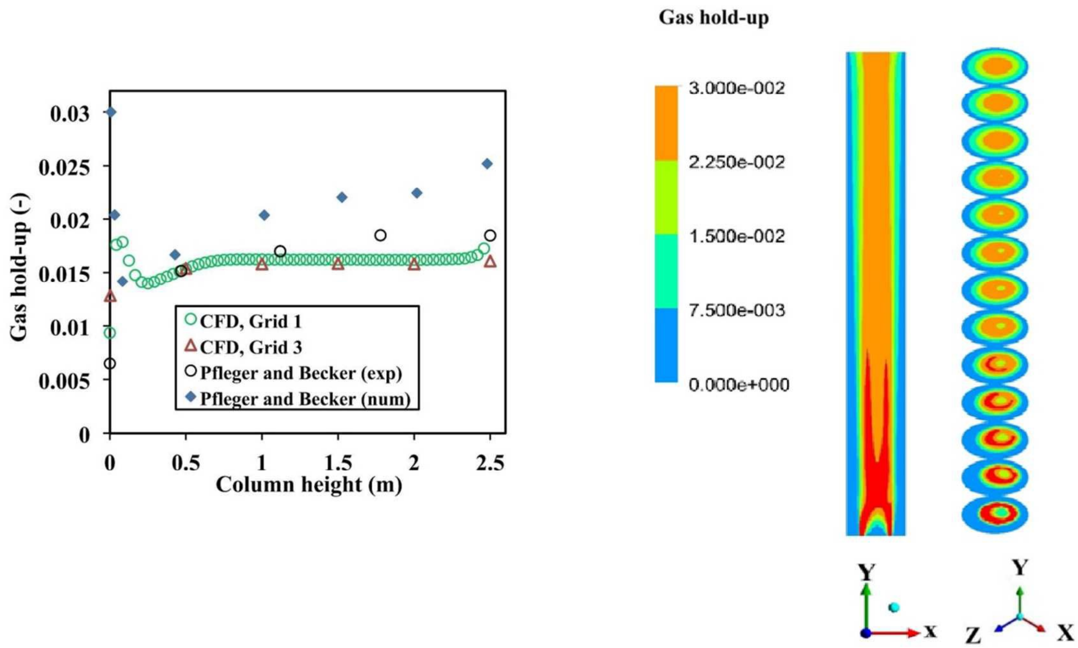

Figure 11 Overall averaged gas hold up for CFD results, Grids 1,3 and those from experiment and simulation in Pfleger and Becker at various heights.

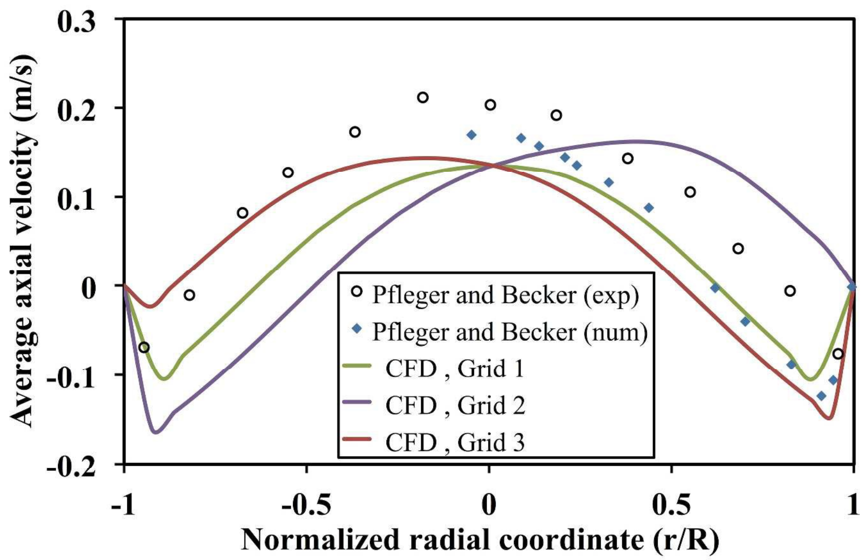

Figure 12 Average axial liquid velocity for CFD, Grids 1-3 and those from experiment and simulation in Pfleger and Becker at height 1.6m.

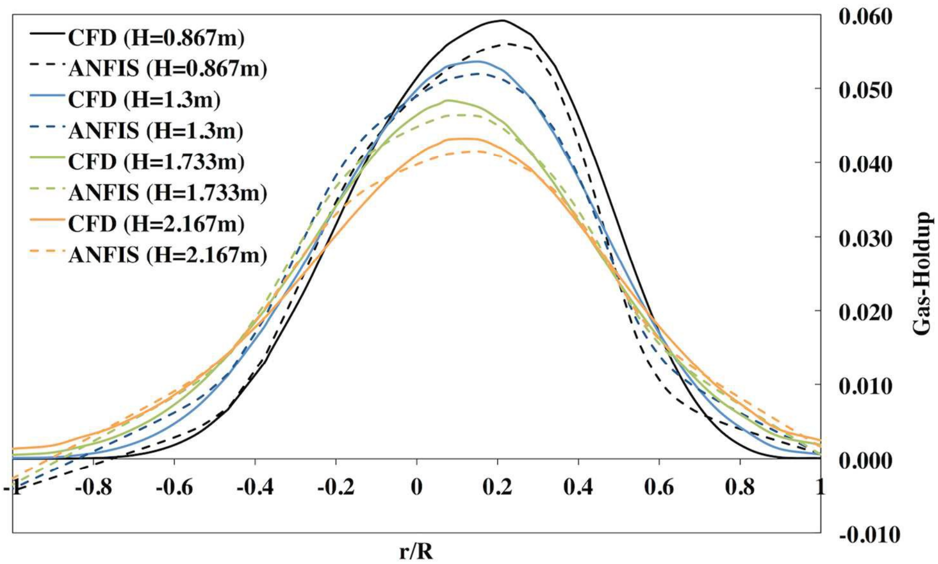

Figure 13(a) Gas hold-up predicted and CFD values in sparger diameter of 0.08m.

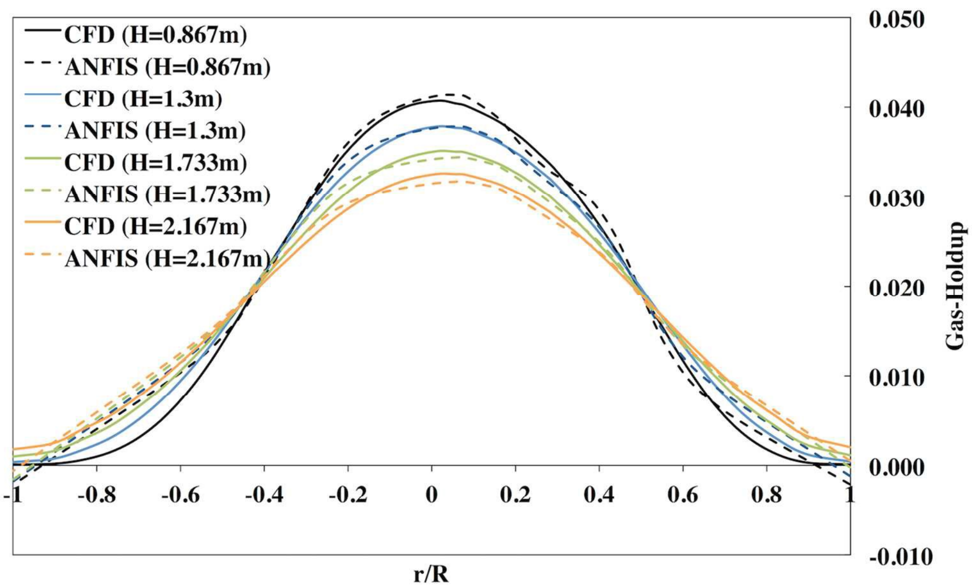

Figure 13(b) Gas hold-up predicted and CFD values in sparger diameter of 0.10m.

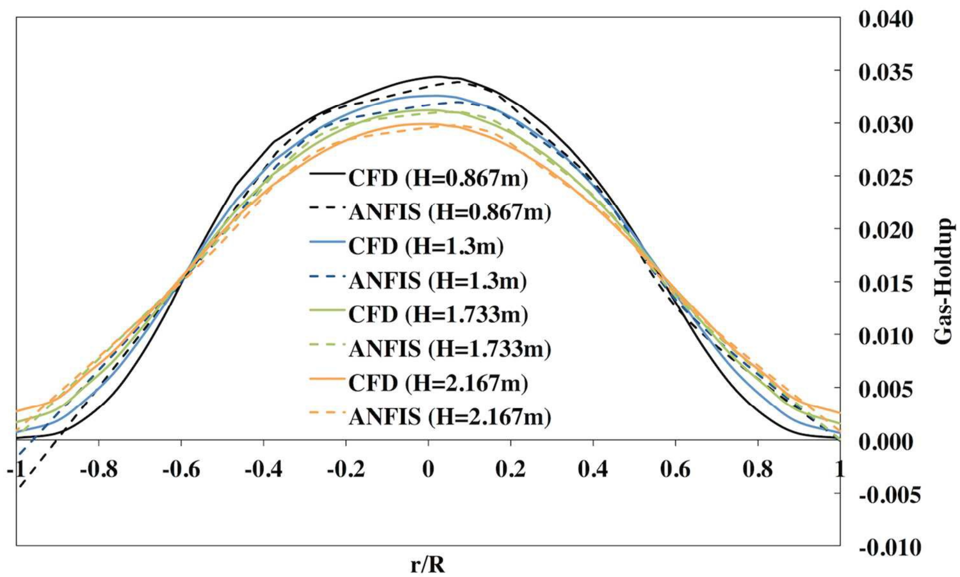

Figure 13 (c) Gas hold-up predicted and CFD values in sparger diameter of 0.12m.

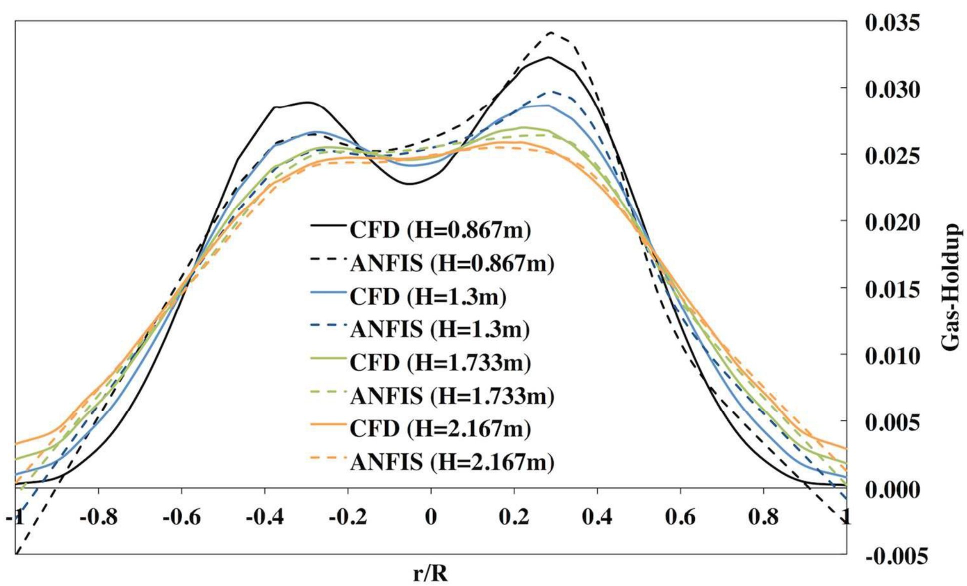

Figure 13 (d) Gas hold-up predicted and CFD values in sparger diameter of 0.14m.

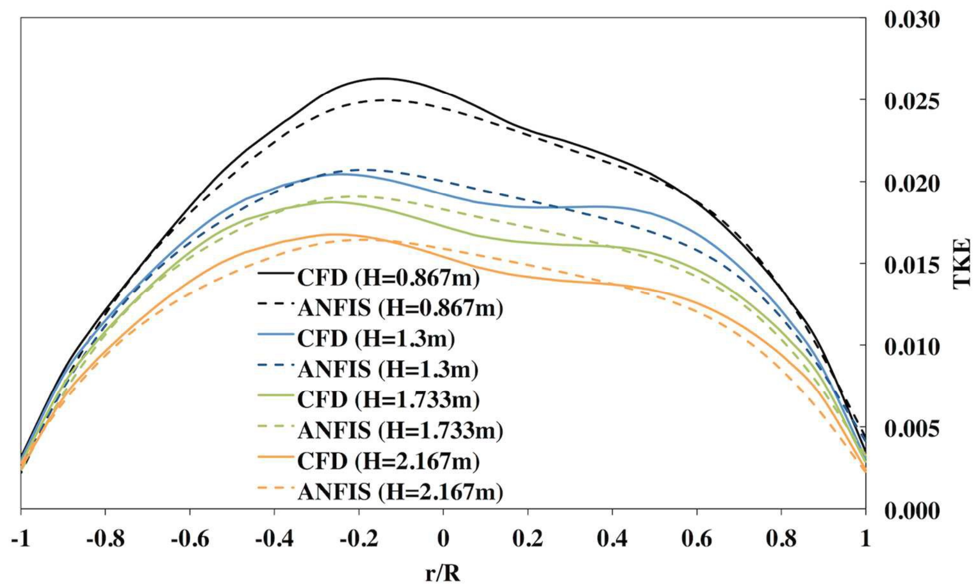

Figure 14 (a) Turbulent kinetic energy predicted and CFD values in sparger diameter of 0.08m.

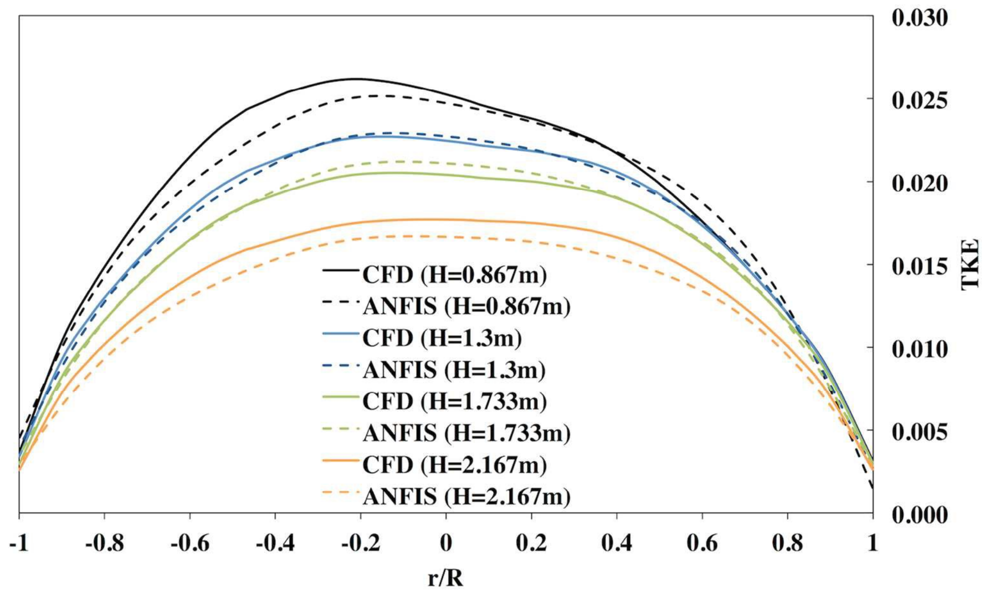

Figure 14 (b) Turbulent kinetic energy predicted and CFD values in sparger diameter of 0.10m.

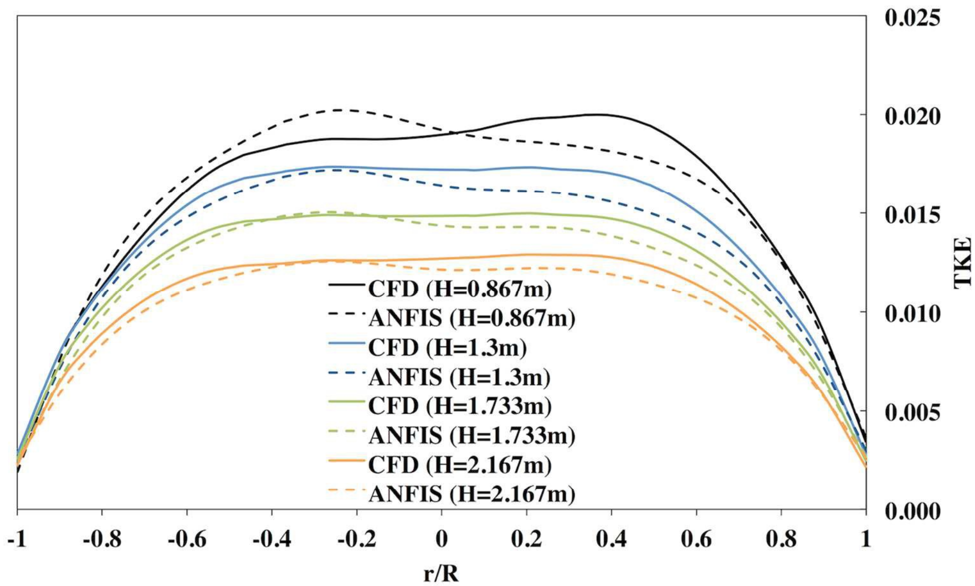

894

895 **Figure 14 (c)** Turbulent kinetic energy predicted and CFD values in sparger diameter of 0.12m.

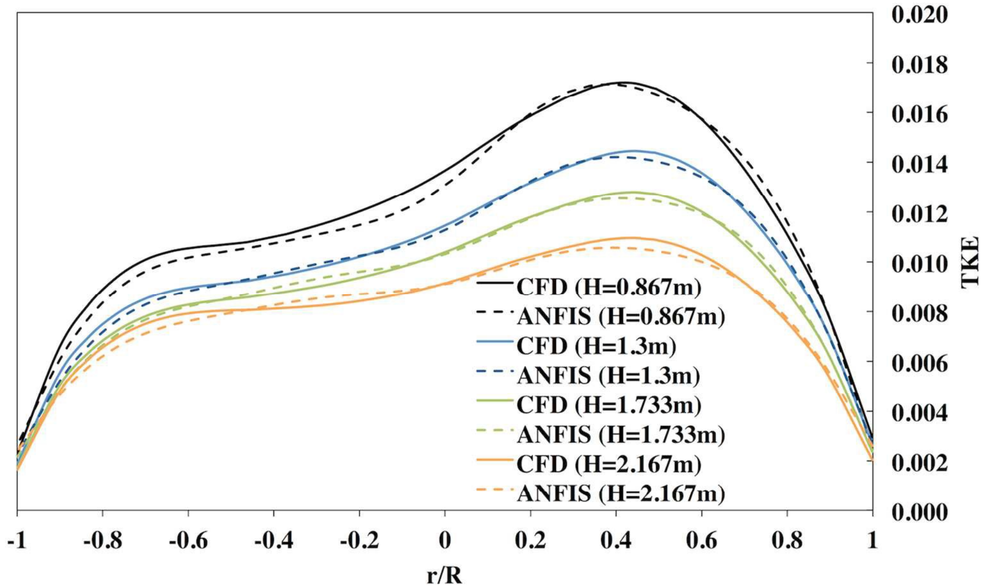

896

897 **Figure 14 (d)** Turbulent kinetic energy predicted and CFD values in sparger diameter of 0.14m.

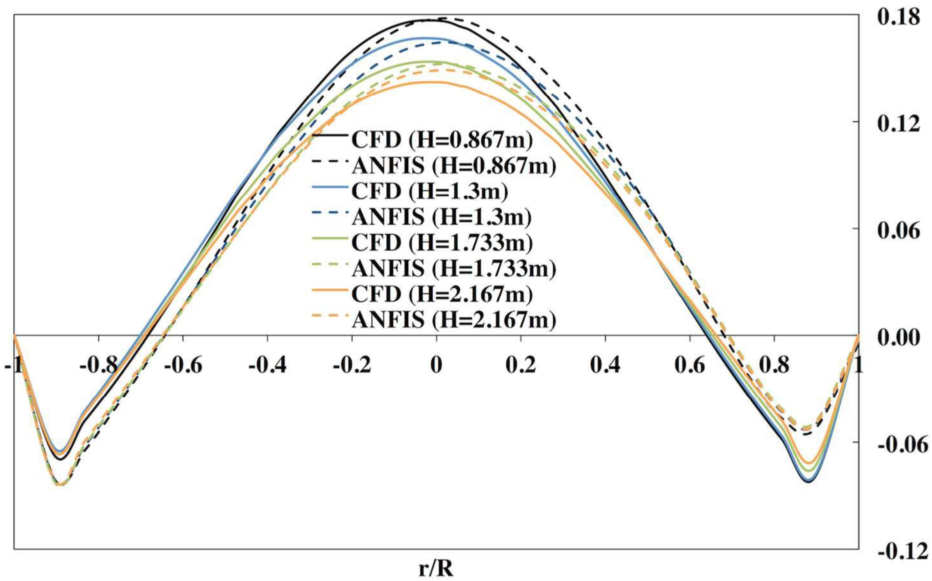

Figure 15(a) Axial velocity predicted and CFD values in sparger diameter of 0.08m.

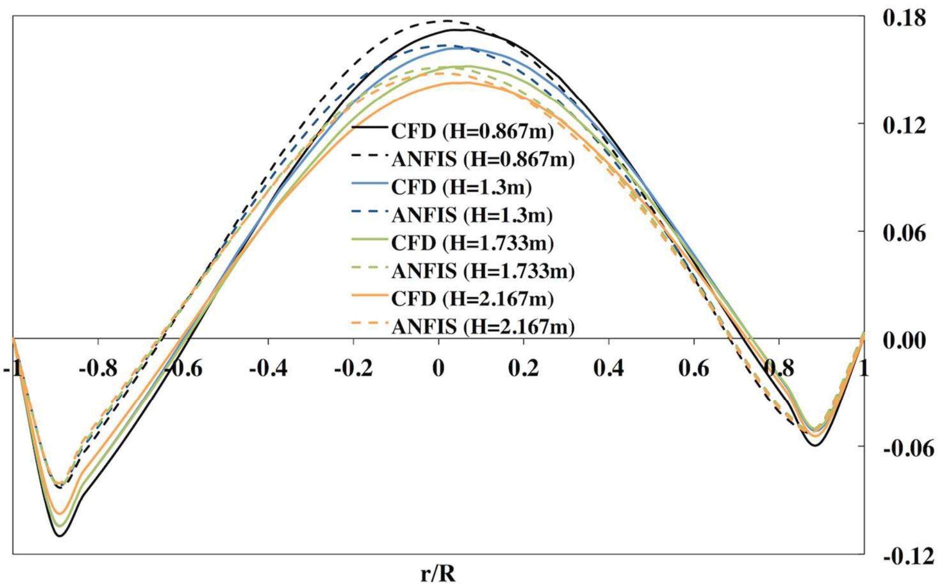

Figure 15(b) Axial velocity predicted and CFD values in sparger diameter of 0.10m.

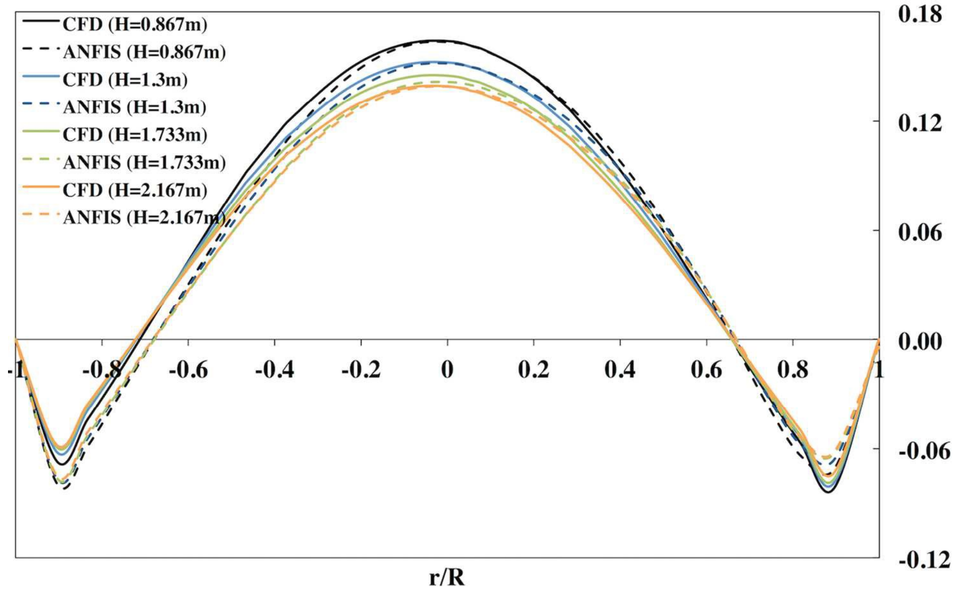

Figure 15(c) Axial velocity predicted and CFD values in sparger diameter of 0.12m.

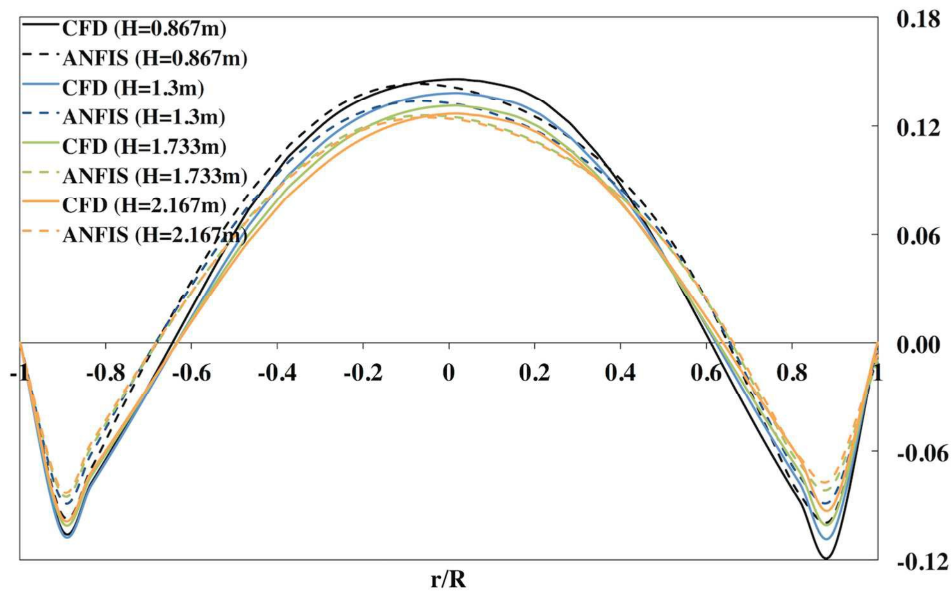

Figure 15(d) Axial velocity predicted and CFD values in sparger diameter of 0.14m.

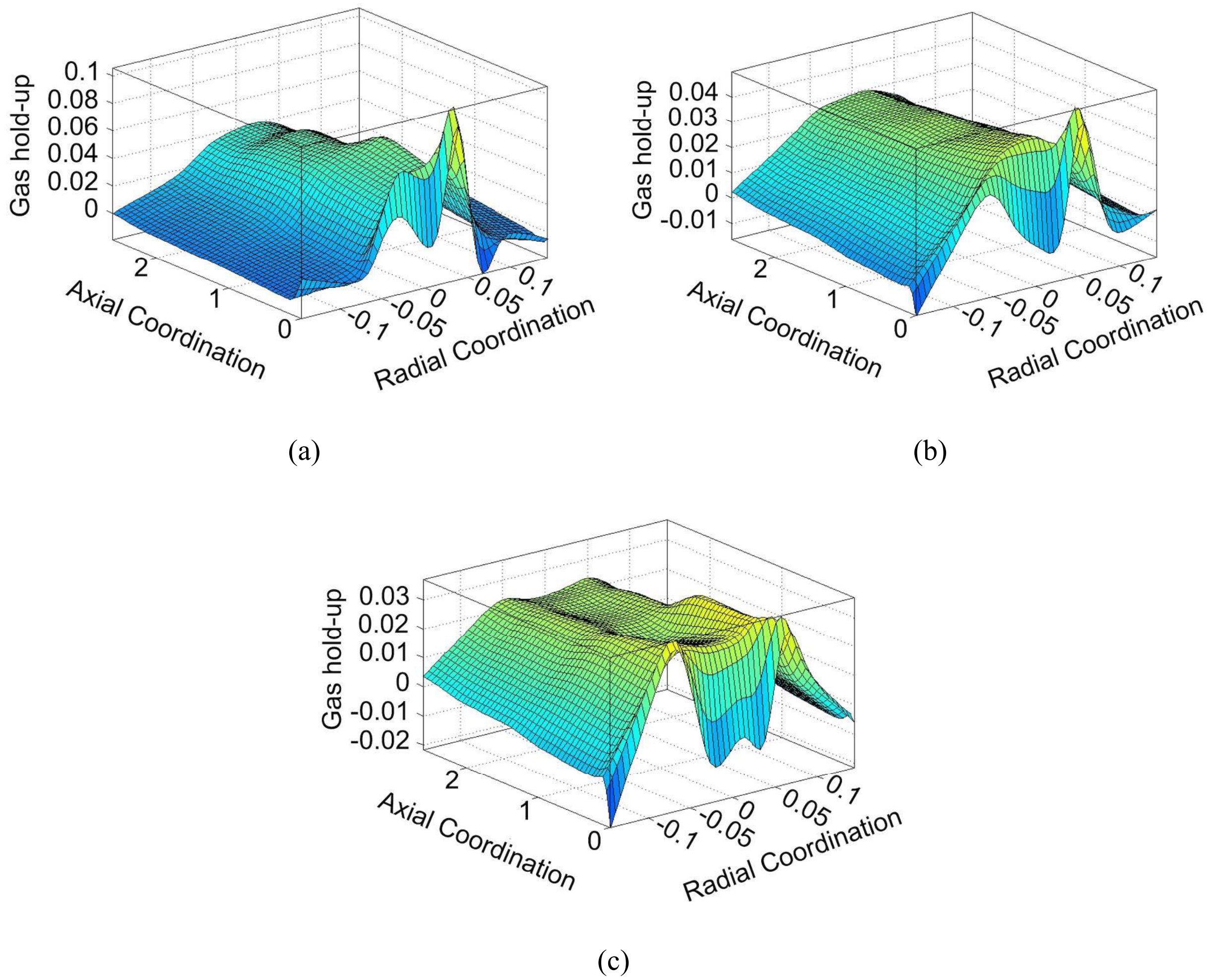

Figure 16 Surface rules of selected ANFIS method in gas hold-up at sparger diameters of (a) 0.085 (b) 0.115 and (c) 0.145.

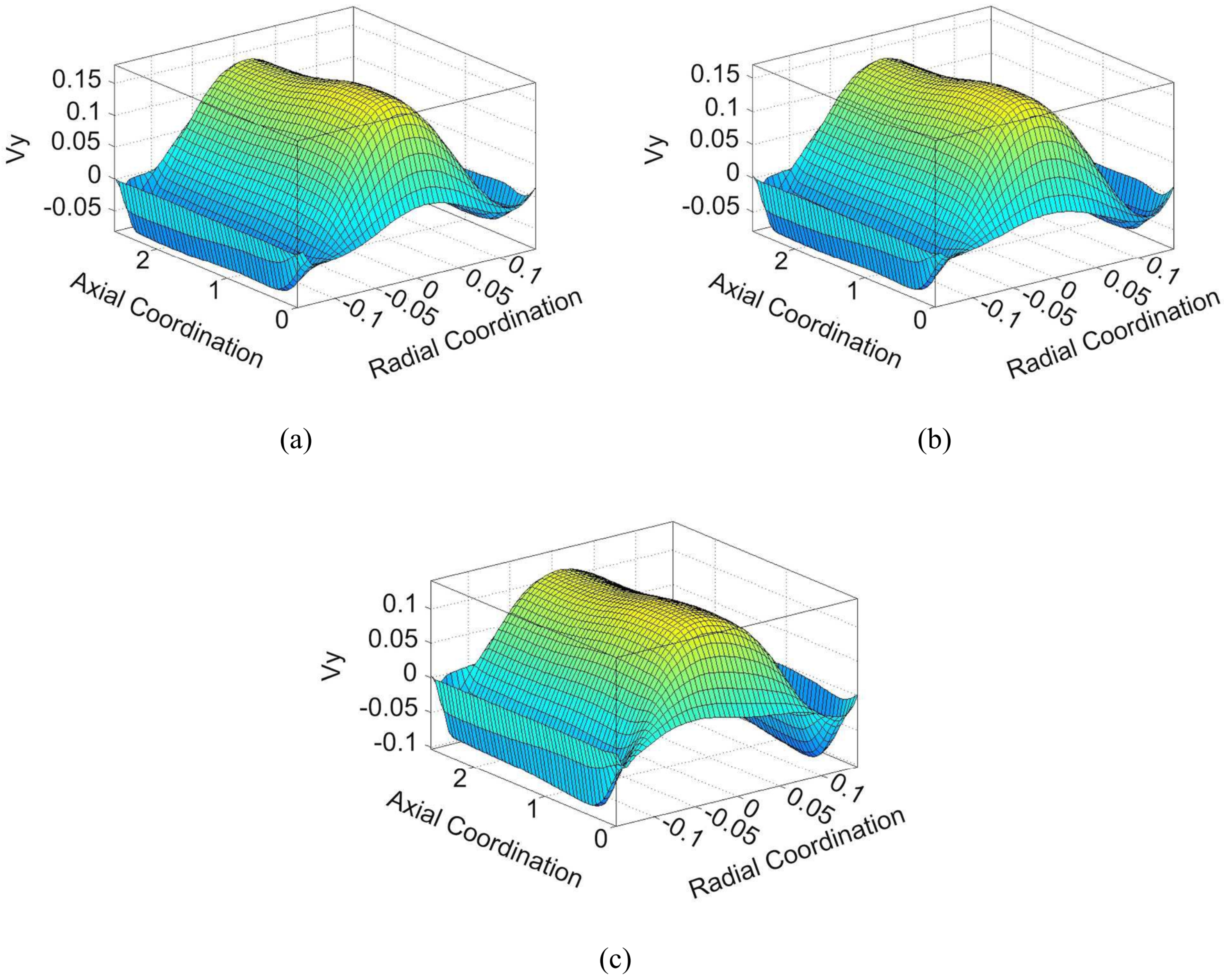

Figure 17 Surface rules of selected ANFIS method in axial velocity at sparger diameters of (a) 0.085 (b) 0.115 and (c) 0.145.

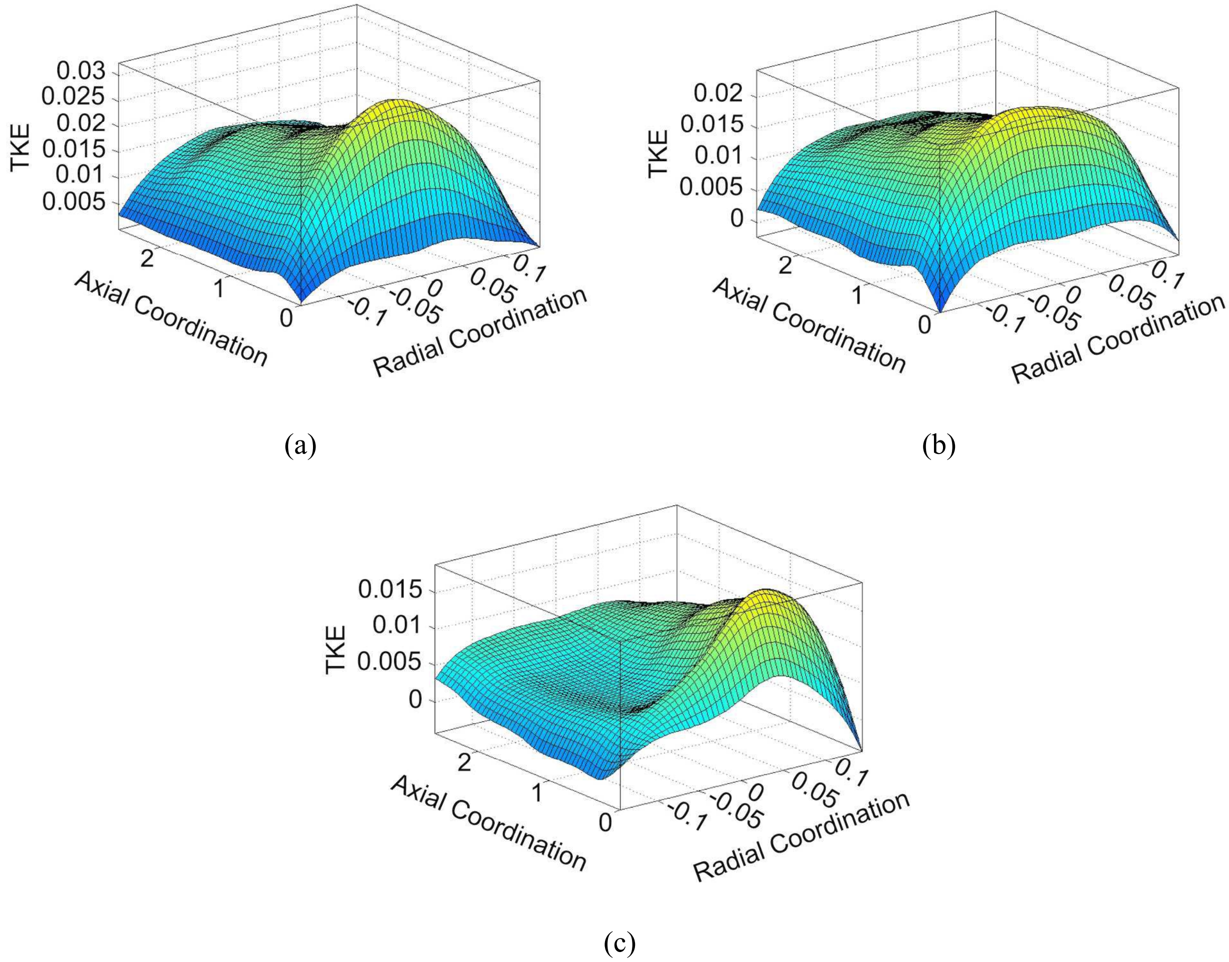

Figure 18 Surface rules of selected ANFIS method in turbulent kinetic energy at sparger diameters of (a) 0.085 (b) 0.115 and (c) 0.145.

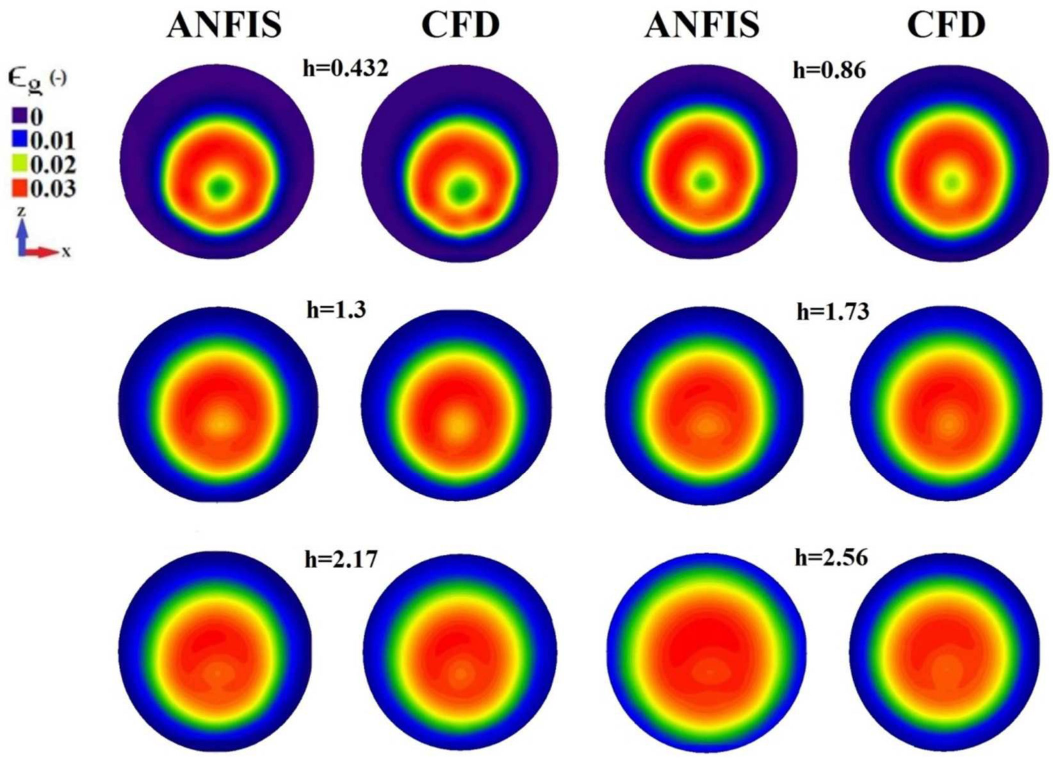

919

920 **Figure 19** Contour of gas hold-up at various column heights for ANFIS and CFD method.

921 .

922

923

924

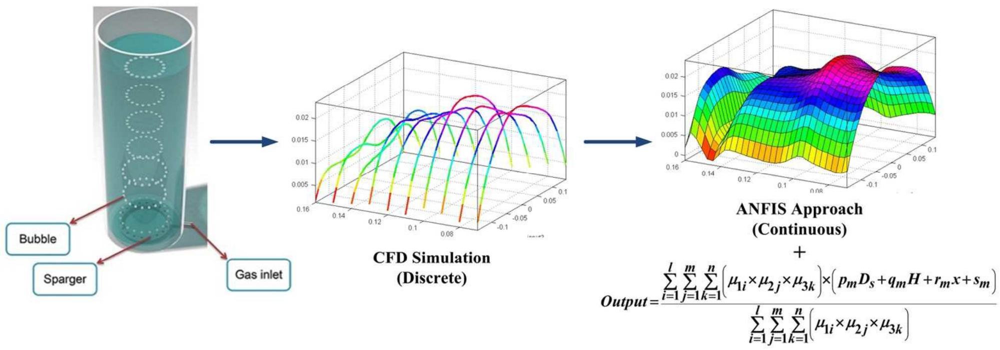

146x51mm (300 x 300 DPI)